Three-Dimensional Discrete Element Method Parallel Computation of Cauchy Stress Distribution over Granular Materials

Beichuan Yan[a], Richard A. Regueiro[a,*]

[a]*Department of Civil, Environmental, and Architectural Engineering*
University of Colorado Boulder

Abstract

The paper presents Cauchy stress tensor computation over parallel grids of Message Passing Interface (MPI) parallel Three-Dimensional (3D) Discrete Element Method (DEM) simulations of granular materials, considering spherical and non-spherical particles. The stress tensor computation is studied for quasi-static and dynamic conditions, and its resulting symmetry or asymmetry is discussed within the context of classical continuum mechanics (CCM), granular materials mechanics (GMM), and micropolar continuum mechanics (MCM). The average Cauchy stress tensor computation follows Bagi's and Nicot's formulations and is verified within MPI parallel 3D DEM simulations involving dynamically-adaptive compute grids. These grids allow calculation of temporal and spatial distributions of stress across granular materials under static and dynamic conditions. The vertical stress component in gravitationally-deposited particle assemblies exhibits non-uniform spatial distributions under static equilibrium, and its zone of maximum value changes during the process of gravitational pluviation and collapse. These phenomena reveal a microstructural effect on stress distribution within granular materials that is attributed to their discrete particulate nature (particle size, shape, gradation, boundary conditions, etc).

Keywords: granular materials, average stress tensor, stress distribution, symmetry and asymmetry, discrete element method, parallel computing

*Corresponding author. Fax: +1-303-492-7317
Email addresses: beichuan.yan@colorado.edu (Beichuan Yan), richard.regueiro@colorado.edu (Richard A. Regueiro)

1. INTRODUCTION

Granular materials may behave mechanically in a discrete or continuous manner, exhibiting solid- or fluid-like properties and transitions in between. Regardless of mechanical response, the underlying particulate nature of granular materials is responsible for their range of behavior and properties. Even with anticipated adoption of exascale computing platforms (with limited access), it will be too computationally expensive to account for every particle (or grain) of a granular material with regard to engineering design, such as building foundations subjected to sand liquefaction, tire/tool interactions with granular soils on the Earth, Moon, or Mars, marine soil anchoring mechanisms, etc. Such simulations would require billions to trillions, if not more, of non-spherical particles within 3D DEM codes, with possible additional coupling to Computational Fluid Dynamics (CFD). As a result, for the foreseeable future, continuum mechanics will likely remain the most efficient modeling framework within which to simulate the range of mechanical behavior and properties that granular materials experience. However, recognizing the deficiencies of a purely continuum approach, multiscale modeling approaches are being developed whereby DEM-CFD codes are hierarchically or concurrently coupled to continuum numerical methods such as the Finite Element Method (FEM) or meshfree methods. For such methods, it is necessary to upscale discrete particle behavior to continuum variables such as stress, strain, stress-rate and strain-rate, etc, within large deformation, nonlinear continuum mechanics, and to do so within a MPI parallel 3D DEM code. Thus, as a first step, the paper focuses on the computation of the Cauchy stress tensor within dynamically-adaptive compute grids associated with an MPI parallel 3D DEM non-spherical particle code *ParaEllip3d* (Yan and Regueiro, 2018b,c,f,a,e). Specifically, the paper focuses on two aspects of the problem:

1. The microstructural definition of the average stress tensor over a particle assembly has been a controversial topic (Weber, 1966; Christoffersen et al., 1981; Rothenburg and Selvadurai, 1981; Bagi, 1996, 1999, 2003; Kuhn, 2003; Bardet and Vardoulakis, 2001; Fortin et al., 2003; De Saxcé et al., 2004; Balevičius and Markauskas, 2007; Nicot et al., 2013; Yan and Regueiro, 2018d), especially when inertial terms are included. In particular, a point of contention has

been whether stress tensor asymmetry should be accounted for or not. Chang and Ma (1991); Huang et al. (2002); Durán et al. (2010) advocated the use of an asymmetric stress tensor, while Cundall and Strack (1979); Durán et al. (2010) suggested negligible stress asymmetry for practical purposes.

2. The computational capability of 3D DEM is limited by two factors: (i) number of particles, and (ii) shape and size distribution that can be simulated. For example, most applications involving complex-shaped (non-spherical) particles such as axisymmetric ellipsoids (Ng, 1994, 2004), three-axis ellipsoids (Yan et al., 2010), poly-ellipsoids (Peters et al., 2009; Zhang et al., 2018), superellipsoids (Wellmann et al., 2008; Delaney et al., 2010), or asymmetrical particles constructed by non-uniform rational Basis-Splines (NURBS) (Lim and Andrade, 2014) constrain their number of particles to tens of thousands, typically not exceeding 100,000. This particle number limitation may cause simulations to miss interesting granular physics that are only observed for greater than 500,000 to many millions (and perhaps billions to trillions) of non-spherical particles.

Recently, Yan and Regueiro (2018d) attempted to clarify the stress tensor definition and its symmetry property by conducting OpenMP (serial-like) 3D DEM simulations for various static, quasi-static, and dynamic cases, such as gravitational deposition, isotropic/oedometer compression, and high-strain-rate (HSR) oedometer impact. They concluded that the stress tensor should be calculated using Bagi's formula (Bagi, 1996, 1999, 2003), not Weber's (Weber, 1966; Christoffersen et al., 1981; Rothenburg and Selvadurai, 1981) or Drescher's formulas (Drescher and De Jong, 1972; Cowin, 1977; Cundall and Strack, 1983), for a particle assembly or representative volume element (RVE) in static equilibrium. They proposed to modify De Saxcé's formula (Fortin et al., 2003; De Saxcé et al., 2004) and Nicot's formula (Nicot et al., 2013), which take into account body forces and inertial terms, by incorporating a *boundary-radius-gap* term, such that these stress definitions are consistent with and converge to Bagi's definition under static conditions. This is important when studying granular phenomena that transition between static, quasi-static, and dynamic conditions.

With regard to computational capabilities, parallel computing of 3D DEM has become an indispensable trend in numerical modeling of granular materials that involve a large number of particles, especially for model-

ing complex-shaped (i.e., non-spherical) particles which require high CPU-demand. There has been considerable interest in developing and utilizing parallel DEM codes in recent years (Henty, 2000; Baugh Jr and Konduri, 2001; Washington and Meegoda, 2003; Maknickas et al., 2006). For example, Vedachalam and Virdee (2011) used LAMMPS (large-scale atomic and molecular massively parallel simulator, developed by Sandia National Laboratories) and LIGGGHTS (LAMMPS improved for general granular and granular heat transfer simulations) to study the motion of snow particles, wherein the snow grains are assumed to be spherical particles 5 mm in diameter. An empirical coefficient of restitution (ratio of rebound velocity to impact velocity) is adopted rather than the strict Hertzian nonlinear contact model, while Mindlin's history-dependent shear model is not considered. Recently, Yan and Regueiro (2018b,c,f,a,e) provided unprecedented parallel 3D DEM simulation capability for complex-shaped particles across five orders of magnitude of simulation scale (i.e., number of particles) on U.S. Department of Defense (DoD) supercomputers using *ParaEllip3d*, a MPI parallel 3D DEM code developed at the University of Colorado Boulder, providing detailed performance analyses including speedup, efficiency, scalability, and granularity. For example, up to 2,048 compute nodes (32,768 cores) are used for simulating 10 million three-axis ellipsoidal particles (equivalent to approximately 1 billion spherical particles in terms of computational demand). They determined that superlinear speedup is a common phenomenon for large scale MPI parallel 3D DEM simulations of complex-shaped particles based upon a spatial domain decomposition algorithm. It was shown to be associated with inherent perfect scalability of 3D DEM; i.e., its memory scalability function is a nonlinearly decreasing function of the number of processors.

Computing the Cauchy stress tensor and its spatial distribution over granular materials does not require parallel computing, per se, but in addition to being able to simulate a large number of particles, it also provides a natural and accurate spatial partitioning boundary using parallel compute grids (spatially-adaptive grids if the parallel algorithm is well designed). In fact, for MPI parallel 3D DEM simulations of complex-shaped particles, the parallel compute grid size can be easily changed such that it can adapt to any characteristic length scale needed in continuum models: it can be much larger than the mean particle diameter, or it can be equivalent to a single particle diameter. Furthermore, the compute grids of MPI parallel 3D DEM provide a natural framework for calculating finite strain measures in granular materials (Zhang and Regueiro, 2015), by tracking the motion of

particles within the grids, therefore making it possible to study stress-strain and stress-strain-rate-form constitutive relations (not covered in the paper).

It should be noted that a proper implementation and application of the average Cauchy stress tensor in a typical spatial domain decomposition parallelism of MPI parallel 3D DEM relies upon the form of stress tensor definition and thus requires careful treatment. For example, if Bagi's formula is adopted, it is not only necessary to collect boundary-particle contact information, but also requires processing particle-particle contact information between adjacent compute grids and define branch vectors accurately, which will be covered in detail in the paper.

The structure of the remainder of the paper is as follows: Section 2 summarizes various analytical formulas for the calculation of the Cauchy stress tensor in granular materials; Section 3 discusses conceptually stress tensor symmetry from the perspective of classical continuum mechanics (CCM), granular materials mechanics (GMM), and micropolar continuum mechanics (MCM); Section 4 presents the MPI parallel computing framework of 3D DEM based upon spatial domain decomposition; Section 5 details the correct algorithm for stress tensor calculation in MPI parallel 3D DEM; Section 6 provides an analysis of stress tensor components calculated using OpenMP 3D DEM; Section 7 provides stress tensor spatial distributions across particle assemblies via MPI parallel 3D DEM; Section 8 examines temporal and spatial distributions of stress during dynamic processes; Section 9 investigates the microstructural effects of particle assemblies on stress distribution; and the last section provides conclusions and outlooks.

2. ANALYTICAL STRESS TENSOR FORMULAS FOR GRANULAR MATERIALS

Weber (1966) proposed a stress tensor definition for granular materials by averaging the particle contact forces in the vicinity of a spatial point. Christoffersen et al. (1981) derived the same formula for stress by volume-averaging the product of contact forces and branch vectors, applying the principle of virtual work. In summary, Weber (1966); Christoffersen et al. (1981); Rothenburg and Selvadurai (1981) calculated the stress tensor using the following formula as,

$$\langle \sigma_{ij} \rangle_{\text{Weber}} = \frac{1}{V} \sum_{c \in I} f_i^c l_j^c \tag{1}$$

where V is the RVE volume, c is the particle contact point, and I is the total number of particle contacts internal to the RVE. The force vector f_i^c is the contact force transmitted at internal particle contact point c, as illustrated in Fig.1(a). The vector l_j^c is the branch vector for internal contact point c which connects the centroids of two adjoining particles.

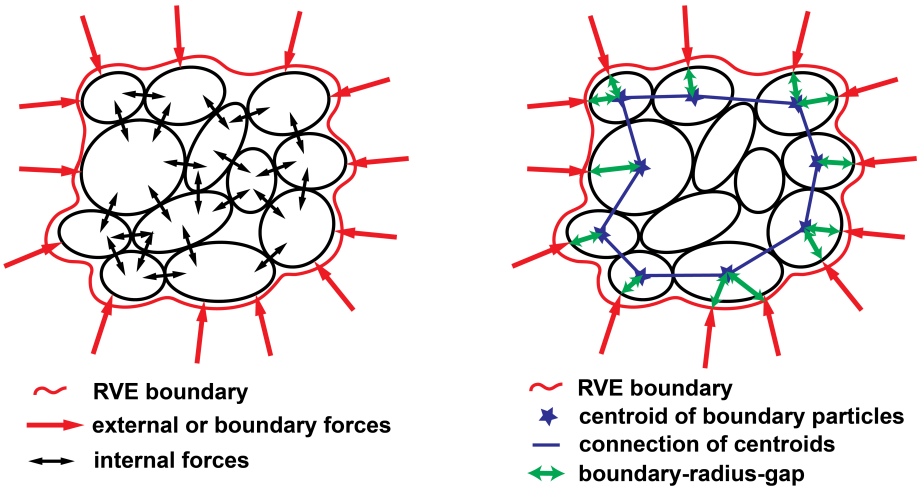

(a) Internal and external forces. (b) Boundary-radius-gap.

Figure 1: Schematic of RVE.

Drescher and De Jong (1972); Cowin (1977); Cundall and Strack (1983) presented a stress definition which considered the relation between a volume average of stress and a surface integral of traction within classical continuum mechanics. Such a definition was made without employing the principle of virtual work as,

$$\langle \sigma_{ij} \rangle_{\text{Drescher}} = \frac{1}{V} \sum_{e \in E} f_i^e x_j^e \tag{2}$$

where E is all particle contacts external to or on the boundary of the RVE, f_i^e is the contact force vector at point e on the RVE boundary, as shown in Fig.1(a), and x_j^e is the current space coordinate vector of contact point e on the boundary.

Bagi (1996) presented definitions of stress and small strain in terms of local, micro-level variables with the help of two complementary geometrical

systems. Bagi (1999) presented the stress tensor definition of particle assemblies with volumetric loads in addition to boundary forces, using clearly-defined branch vectors. For internal contacts, a branch vector connects the centroids of two particles, and for external contacts, a branch vector points from the centroid of a boundary particle to its external contact point. The stress tensor definition included both internal and external contact forces such that (Bagi, 2003),

$$\langle \sigma_{ij} \rangle_{\text{Bagi}} = \frac{1}{V} \left(\sum_{c \in I} f_i^c l_j^c + \sum_{e \in E} f_i^e l_j^e \right) \tag{3}$$

where f_i^e is the contact force vector at point e on the RVE boundary, and l_j^e is the branch vector associated with external contact point e, also called *boundary-radius gap*, which points from the centroid of a boundary particle to the external contact point e, as illustrated in Fig.1(b).

Bardet and Vardoulakis (2001) noted that stress tensor symmetry has significance in computational granular mechanics, particularly for DEM simulations employing dynamic relaxation (DR) to solve the dynamic equilibrium equations for quasi-static problems. They concluded that computed stress tensor asymmetry implied inaccurate calculation and/or lack of static equilibrium. If correct, their conclusion would also be applicable to dynamic simulations which eventually reach static equilibrium.

Fortin et al. (2003); De Saxcé et al. (2004) constructed an average Cauchy stress tensor in integral form which takes into account the contact reaction forces and body forces as,

$$\langle \sigma_{ij} \rangle_{\text{De Saxcé}} = \frac{1}{V} \left(\sum_{c \in \{I \cup E\}} x_i^c f_j^c + \int_V x_i \rho \Big(g_j - a_j \Big) dV \right) \tag{4}$$

where f_j^c denotes either an internal or boundary contact force vector at point c, g_j is the gravitational acceleration vector, a_j is the acceleration vector, and x_j is the current spatial coordinate vector within V. It was noted that the constructed stress tensor is automatically symmetric and invariant by translation. De Saxcé et al. (2004) also presented a rigorous proof of stress tensor symmetry by applying the balance of angular momentum.

Nicot et al. (2013) studied the stress tensor definition based on an equivalent continuum, but using different decomposition of dynamic contributions.

They concluded that the stress tensor can be expressed as a sum of two contributions: (i) the standard term by Love-Weber formula for quasi-statics; and (ii) dynamic terms resulting from rotational particle velocities and accelerations. It is interesting to observe from their numerical simulation of silo discharge that the stress inertial terms are an order of magnitude lower than the static stress terms. The balance of linear momentum is relied upon in their derivation, whereas the balance of angular momentum is not. Nicot's formula is as follows,

$$\langle\sigma_{ij}\rangle_{\text{Nicot}} = \frac{1}{V}\sum_{c\in I} f_i^c l_j^c - \frac{1}{V}\sum_{p\in\{I\cup E\}}\left(\varepsilon_{ikl}\dot{\Omega}_k^p\chi_{jl}^p + \Omega_i^p\Omega_k^p\chi_{jk}^p - (\Omega^p)^2\chi_{ij}^p\right) \quad (5)$$

where p denotes a particle within $I\cup E$, ε_{ikl} is the permutation symbol, Ω_k^p denotes the angular velocity vector of particle p and Ω^p its magnitude, and χ_{ij}^p is the inertial tensor for particle p. The angular velocity, angular acceleration, and inertial tensor are written with respect to the global coordinate system (GCS) in Eq.(5), and must be converted to GCS if first calculated in a local coordinate system (LCS) associated with particle p.

Yan and Regueiro (2018d) proved the so-called *equation of stress equivalence*, and concluded that the stress tensor for a particle assembly or RVE which is subjected to boundary forces and gravity forces in static equilibrium should be calculated via Bagi's formula, not Weber's formula. As a result, Yan and Regueiro (2018d) derived a so-called *modified Nicot's formula* as,

$$\begin{aligned}\langle\sigma_{ij}\rangle_{\text{Nicot-2}} =& \frac{1}{V}\left(\sum_{c\in I} f_i^c l_j^c + \sum_{e\in E} f_i^e l_j^e\right)\\ &-\frac{1}{V}\sum_{p\in\{I\cup E\}}\left(\varepsilon_{ikl}\dot{\Omega}_k^p\chi_{jl}^p + \Omega_i^p\Omega_k^p\chi_{jk}^p - (\Omega^p)^2\chi_{ij}^p\right),\end{aligned} \quad (6)$$

and so-called *modified De Saxcé's formula* as,

$$\langle\sigma_{ij}\rangle_{\text{De Saxcé-2}} = \frac{1}{V}\left(\sum_{c\in I} f_i^c l_j^c + \sum_{e\in E} f_i^e l_j^e\right) - \frac{1}{V}\left(\int_V x_i\rho a_j dV\right), \quad (7)$$

by incorporating the boundary-radius-gap term. The *modified Nicot's formula* and *modified De Saxcé's formula* share two important features: (i) the gravity term vanishes, and (ii) both converge to Bagi's formula under static conditions.

3. SYMMETRY OF STRESS TENSOR IN GRANULAR MATERIALS

3.1. Stress tensor in classical continuum mechanics (CCM)

In CCM, the balance of linear momentum and angular momentum for a continuous body are expressed in Eq.(8) and (9), respectively, as,

$$\int_{\partial V} \boldsymbol{t} dS + \int_V \boldsymbol{f} dV = \boldsymbol{0}, \tag{8}$$

$$\int_{\partial V} \boldsymbol{x} \times \boldsymbol{t} dS + \int_V \boldsymbol{x} \times \boldsymbol{f} dV = \boldsymbol{0}, \tag{9}$$

$$\boldsymbol{n}\boldsymbol{\sigma} = \boldsymbol{t} \text{ or } n_j \sigma_{ji} = t_i \tag{10}$$

where $\boldsymbol{x}$ denotes current coordinate in V or on ∂V, $\boldsymbol{f}$ is the body force per unit volume, $\boldsymbol{f} = \rho(\boldsymbol{g} - \boldsymbol{a})$, including both gravity acceleration $\boldsymbol{g}$ and inertial acceleration $\boldsymbol{a}$, ρ is the mass density, and $\boldsymbol{t}$ is the traction on ∂V. Equation (10) represents Cauchy's stress theorem and provides the definition of the Cauchy stress tensor in a continuous body.

It is well known that on the basis of Eq.(10), $\sigma_{ij} = \sigma_{ji}$ if Eq.(8) and (9) are satisfied simultaneously; $\sigma_{ij} \neq \sigma_{ji}$ if Eq.(9) is not satisfied (typically because of the existence of external moment or imbalance of angular momentum). Equation (9) implies that there is no stress couple or local rotational acceleration within CCM, whereas they exist in MCM. In essence, the balance of angular momentum of an infinitesimally-small differential volume element dv within a classical continuum body ensures that there exists no "external" or unbalanced moment on that element.

3.2. Stress tensor in granular materials mechanics (GMM)

De Saxcé et al. (2004) proved Cauchy stress tensor symmetry utilizing the equations of balance of linear and angular momenta in CCM. Note that the modified De Saxcé's formula in Eq.(7) reduces to Bagi's formula for static equilibrium, so the proof of Cauchy stress symmetry in terms of Bagi's formula is incorporated as well. The proof is briefly summarized.

The balance of linear and angular momenta are expressed in index notation as,

$$\int_{\partial V} t_i dS + \int_V f_i dV = 0, \tag{11}$$

$$\int_{\partial V} (x_i t_j - x_j t_i) dS + \int_V (x_i f_j - x_j f_i) dV = 0 \text{ for } i \neq j, \tag{12}$$

and the average stress is thus defined as,

$$\langle \sigma_{ij} \rangle := \frac{1}{V} \left(\int_{\partial V} x_i t_j dS + \int_V x_i f_j dV \right). \tag{13}$$

Then, if σ_{ij} is symmetric, we have,

$$\langle \sigma_{ij} \rangle - \langle \sigma_{ji} \rangle = \frac{1}{V} \left(\int_{\partial V} (x_i t_j - x_j t_i) dS + \int_V (x_i f_j - x_j f_i) dV \right) = 0 \tag{14}$$

It must be emphasized that Eq.(14) may not hold in GMM or MCM. For example, it is possible to show that the following equation holds for a particle assembly or RVE in GMM,

$$\sum_{c \in I} \boldsymbol{l}^c \times \boldsymbol{f}^c + \sum_{e \in E} \boldsymbol{l}^e \times \boldsymbol{f}^e = \sum_{p \in \{I \cup E\}} \boldsymbol{I}^p \dot{\boldsymbol{\Omega}}^p, \tag{15}$$

where $\boldsymbol{I}^p$ denotes the moment of inertial tensor of particle p. For discussion purposes, we assign $\boldsymbol{\Psi} := \sum_{p \in \{I \cup E\}} \boldsymbol{I}^p \dot{\boldsymbol{\Omega}}^p$. Hence, with Eqs.(14) and (15), the shear terms of stress take the following form in GMM:

$$\begin{aligned} \sigma_{23} - \sigma_{32} &= \frac{1}{V} \Psi_1, \\ \sigma_{31} - \sigma_{13} &= \frac{1}{V} \Psi_2, \\ \sigma_{12} - \sigma_{21} &= \frac{1}{V} \Psi_3, \end{aligned} \tag{16}$$

where Ψ_1, Ψ_2 and Ψ_3 are the three components of $\boldsymbol{\Psi}$. This means that in a particle assembly or RVE the average stress tensor could be asymmetric if any particle exhibits angular acceleration, which is highly likely during dynamic loading such as gravitational pluviation.

3.3. Stress tensor in micropolar continuum mechanics (MCM)

In MCM, the balance of angular momentum does not necessarily lead to symmetry of the Cauchy stress tensor. In fact, the Cauchy stress tensor is asymmetric generally in MCM, and the imbalance of angular momentum of CCM is generalized to include additional terms (surface couple, body couple, and intrinsic spin) such that they become balanced. Therefore, the average

stress tensor calculated using Eq.(13) may not be symmetric. In MCM, the balance of angular momentum is stated as (Eringen, 1968),

$$e_k \left[\sigma_{[ij]} - m_{l[ji],l} + \rho(\ell_{[ji]} - \omega_{[ji]})\right] = 0, \tag{17}$$

where e_k is a coefficient such that $e_k = 1$ for $k = 1, 2, 3$ $(i \neq j \neq k)$, the skew part is $\sigma_{[ij]} = (\sigma_{ij} - \sigma_{ji})/2$, m_{lji} is the higher-order couple stress, $\rho\ell_{ji}$ is the body couple force, and $\rho\omega_{ji}$ is the micro-spin inertia, defined respectively as,

$$\begin{aligned}
(m_{lji}n_l)da &:= \int_{da} \sigma_{lj}^{(\alpha)} \xi_i^{(\alpha)} n_l^{(\alpha)} da^{(\alpha)}, \\
(\rho\ell_{ji})dv &:= \int_{dv} \rho^{(\alpha)} f_j^{(\alpha)} \xi_i^{(\alpha)} dv^{(\alpha)}, \\
(\rho\omega_{ji})dv &:= \int_{dv} \rho^{(\alpha)} \ddot{\xi}_j^{(\alpha)} \xi_i^{(\alpha)} dv^{(\alpha)},
\end{aligned} \tag{18}$$

where $\sigma_{lj}^{(\alpha)}$ is the symmetric Cauchy stress of micro-element α, $\xi_i^{(\alpha)}$ is the relative position vector of micro-element α, $\rho^{(\alpha)}$ is the mass density of micro-element α, $f_j^{(\alpha)}$ is the body force per unit mass on micro-element α, and $n_l^{(\alpha)}$ is the unit normal vector on micro-element α. Note that micro-element α within MCM may be a single particle or cluster of particles (Eringen, 1968). Expressing Eq.(17) for $k = 1, 2, 3$, respectively, we have,

$$\begin{aligned}
\sigma_{23} - \sigma_{32} &= \rho(\omega_{32} - \omega_{23}) - \rho(\ell_{32} - \ell_{23}) - (m_{l32,l} - m_{l23,l}) \\
\sigma_{31} - \sigma_{13} &= \rho(\omega_{13} - \omega_{31}) - \rho(\ell_{13} - \ell_{31}) - (m_{l13,l} - m_{l31,l}) \\
\sigma_{12} - \sigma_{21} &= \rho(\omega_{21} - \omega_{12}) - \rho(\ell_{21} - \ell_{12}) - (m_{l21,l} - m_{l12,l}).
\end{aligned} \tag{19}$$

It can be seen that if the skew parts of the micro-spin inertia tensor $\rho\boldsymbol{\omega}$, body force couple $\rho\boldsymbol{\ell}$, and divergence of couple stress (div$\boldsymbol{m}$) are zero, then the Cauchy stress tensor is symmetric. Otherwise, if any of these terms are non-zero, such as the skew part of the micro-spin inertia tensor $\rho\boldsymbol{\omega}$, the Cauchy stress will be asymmetric, such as shown in Eq.(16) for GMM.

In CCM, the Cauchy stress tensor is symmetric under static and dynamic conditions. In MCM, the Cauchy stress tensor becomes symmetric only when the right-hand-side terms in Eq.(19) are zero, such as for static conditions and when body force couple and divergence of couple stress are negligible. That is why Bagi's formula is chosen under static conditions: stress calculated from Bagi's formula satisfies symmetry whether the granular material is treated as CCM, or special conditions ($\rho\boldsymbol{\ell} \approx \mathbf{0}$ and div$\boldsymbol{m} \approx \mathbf{0}$) for MCM.

To evaluate the degree of asymmetry of the stress tensor, we define a quantity, *relative asymmetry index* (RAI), as the ratio of L_2-norm of the skew-symmetric part to the symmetric part with diagonal elements set to zero, such that,

$$RAI = \frac{\left(\frac{1}{2}\left(\langle\sigma_{ij}\rangle - \langle\sigma_{ij}\rangle^T\right)\right)^{L_2-norm}}{\left(\frac{1}{2}\left(\langle\sigma_{ij}\rangle + \langle\sigma_{ij}\rangle^T\right)\right)^{L_2-norm}_{diag=0}}. \tag{20}$$

3.4. Stress wave propagation

In dynamic simulations, forces exerted on the boundary of the particle assembly in each time step are not felt instantaneously by the interior particles because it takes a certain number of time steps for the DEM system to transmit boundary forces to the interior particles (for the wave to propagate through the assembly). No doubt this also holds true for quasi-static simulations, to a certain degree. When this stress wave effect is pronounced, the balance of linear and angular momenta are not satisfied (classically) at a discrete instant in time, namely, Eq.(12) does not hold, and the stress tensor is asymmetric.

More simply, when a dynamic boundary condition (force, displacement, or combination thereof) is applied to a particle assembly, it may exert an external moment, and in turn impose an imbalance of angular momentum; the particle assembly undergoes an overall "rotational" acceleration, or so-called "intrinsic spin." This phenomenon does not exist for an infinitesimally-small continuum point with differential volume dv in CCM, for which it always holds that $\sigma_{ij} = \sigma_{ji}$ because the balance of angular momentum is satisfied. In MCM, the differential volume dv has *length*, as indicated in Eqs.(17)-(19).

The overall "rotation" or "intrinsic spin" of a particle assembly may not be easily observed macroscopically. For example, it exists during oedometer/uniaxial strain in compression, for which the specimen only undergoes macroscopic axial strain. In fact, any form of deformation of a granular material will include macroscopic rotation (or a moment due to constraint on rotation), which is an essential difference from CCM. How to define rotational effects on the stress tensor computation will rely on MCM, and this is beyond the scope of the paper.

4. PARALLEL COMPUTING FOR 3D DEM

4.1. Four-step design and link-block

The four-step design paradigm proposed by Foster (1995) for MPI parallelization was followed for the design of the MPI parallel 3D DEM code *ParaEllip3d*: partitioning, communication, agglomeration, and mapping. The computational spatial domains are divided via the link-cell (LC) method into equal-sized cubical cells of length not smaller than the diameter of the largest particle, illustrated in Fig.2(a).

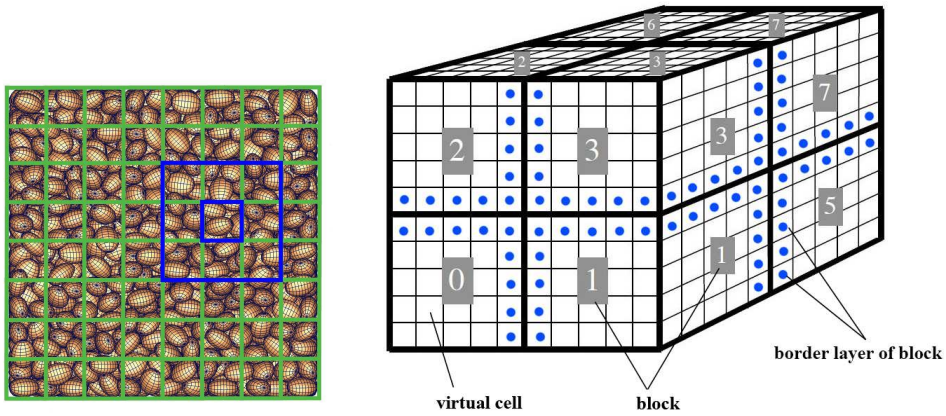

(a) link-cell algorithm, a cell having 26 neighbors in 3D.

(b) Schematic of link-blocks, virtual cells, and border layers.

Figure 2: Link-cell to link-block algorithms.

We extend the link-cell (LC) method to a link-block (LB) technique in MPI parallel 3D DEM. With introduction of LB, Foster's four-step paradigm can be readily applied in designing a parallel algorithm in DEM. **Partitioning:** The computational domain is divided into blocks. Each block may consist of many virtual cells. In Fig.2(b), there are 8 blocks numbered from 0 to 7, each containing 5 x 5 x 5 small virtual cells. The size of the virtual cells may be chosen to be the maximum diameter of the discrete particles. **Communication:** Each cell, as a primitive task unit, can communicate with 26 possible surrounding ones to determine contact detection. However, the communication mechanism may change after agglomeration. **Agglomeration:** By combining 5 x 5 x 5 virtual cells into a block, communication overhead is lowered, such that each block only needs to communicate with neighboring blocks through border/ghost layers (BL), which are virtual cells

marked by blue dots in Fig.2(b). Note that each block communicates with 26 possible BLs, i.e., 6 surface BLs, 12 edge BLs, and 8 vertex BLs. **Mapping:** There are a number of choices for mapping a block of particles to a core, a CPU, multiCPUs within a node, or even a whole node. Very often each block is mapped to a whole compute node.

4.2. Interblock communication

In Fig.2(b), a border/ghost layer is not limited to constructing a surface layer between two adjacent blocks, as there are other forms. For example, block 3 communicates with block 1 through a surface border layer, with block 0 through an edge border layer, and with block 4 through a vertex border layer, as shown in Fig.2(b).

A "patch" test is designed using 162 ellipsoidal particles. The particle assembly is composed of two layers of 81 particles, gravitationally-deposited into a rigid container, illustrated in Fig.3(a). The container is partitioned into four blocks separated by blue dashed lines shown in Fig.3(b), which also represents the initial configuration of the randomly-sized particles as shown from a top view.

Each block is mapped to and computed by an individual process, so there are four processes, p0 to p3. Each process needs to communicate with other processes to determine its own boundary conditions. For example, process p3 needs to know those particles from process p1 that are enclosed by the purple rectangular box, those from process p2 enclosed by the red rectangular box, and those from process p0 enclosed by the green square box. A detailed movie records how those particles move across the borders and collide with particles from other blocks, and it reveals that each process is able to determine its boundary conditions accurately. The overall motion of the 162 particles through parallel computing is observed to be the same as that observed in an OpenMP computation.

4.3. Load balance and adaptive compute grids

In MPI parallel computing it is important to maintain load balance between processes; otherwise, some processes are busy computing while others could be hungry awaiting tasks. To this end, dynamically-adaptive compute grids are developed. Figure 4 demonstrates a simulation of particles falling into a container via gravity, whereby the compute grids (marked by green lines) dynamically follow the particle motions and redistribute across space.

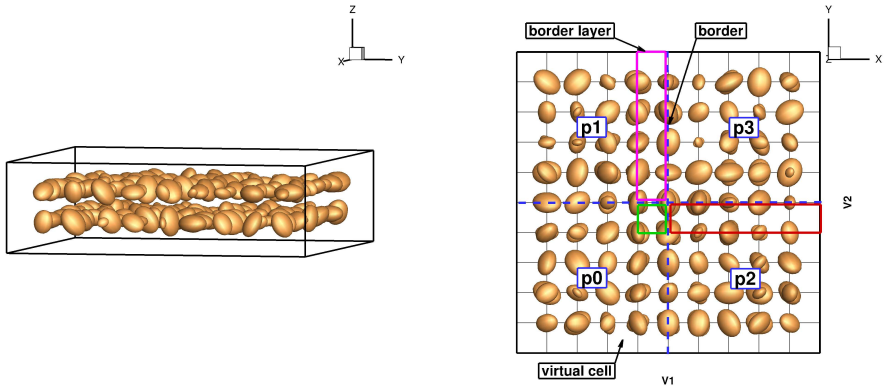

(a) 3D view of initial configuration.

(b) Top view of initial configuration.

(c) Top view at time $t1$ during simulation.

(d) Top view at time $t2$ during simulation.

Figure 3: Illustration of interblock communication.

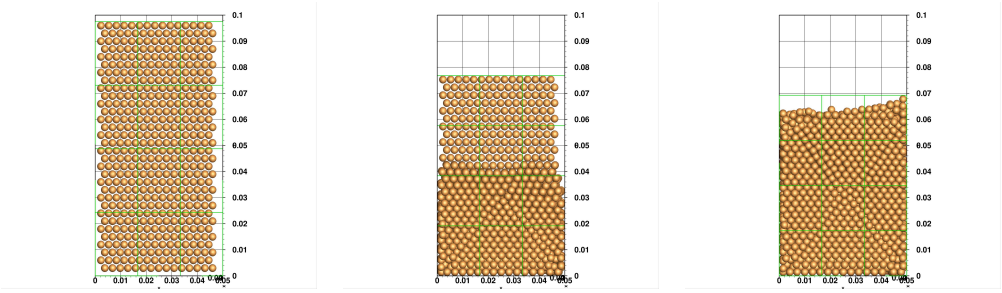

(a) Initial configuration of particle pluviation.

(b) Middle stage of particle pluviation.

(c) Final stage of particle pluviation.

Figure 4: Dynamically-adaptive compute grids that achieve efficient load balance.

4.4. Particle-boundary interaction

The MPI parallel 3D DEM code *ParaEllip3d* not only needs to gather particle data from all processes, but also needs to collect particle-boundary interaction data from those boundary processes. As shown in Fig.4, in order to obtain particle-boundary interaction data on the bottom and four sides of the top-open rigid container, relevant parallel processes must be identified, collected, and communicated to the root process for data merging.

5. STRESS TENSOR IMPLEMENTATION IN PARALLEL DEM

Yan and Regueiro (2018d) have pointed out that the stress tensor should be calculated via Bagi's formula, not Weber's formula or Drescher's formula in static equilibrium. They suggested using the modified Nicot's formula in dynamic simulations, which takes into account inertial terms of particle rotational velocities and accelerations. The stress calculated using the modified Nicot's formula converges to that calculated by Bagi's formula, under static conditions. These two formulas are chosen and implemented in *ParaEllip3d* for stress tensor calculation.

Bagi's formula includes internal contact forces (correspondingly, internal branch vectors) and external contact forces (correspondingly, external branch vectors). These two parts are not necessarily differentiated in serial computing of 3D DEM. However, they must be distinguished in parallel computing in order to implement correct stress tensor calculations.

Figure 5 illustrates a particle assembly structure in parallel computing of DEM. As an example, process p0 only owns black particles that are assigned

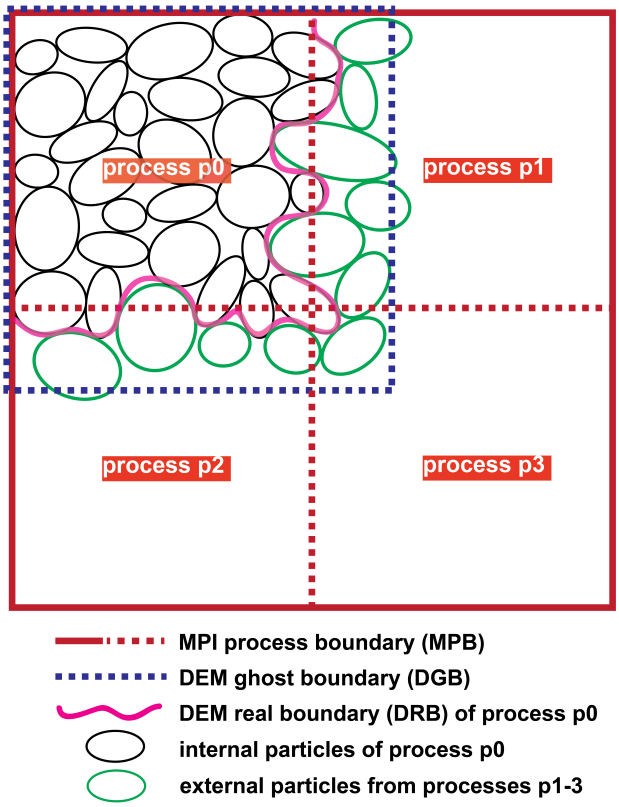

Figure 5: Internal and external particles of a MPI process.

to it at the stage of one-time global partitioning. During the stage of MPI transmission, p0 receives green particles from adjacent processes p1-3. At the stage of neighbor search and contact resolution, p0 actually owns both black and green particles, but it does not need to distinguish black ones from green ones for contact force computation. Nevertheless, at the stage of stress tensor calculation, the black particles are internal particles, and the green particles are external particles, which must be treated differently according to Bagi's formula in Eq.(3).

For any contact-pair consisting of two particles that has been detected, if both particles are "black," then they are treated as an internal contact-pair and computed by the first term of Eq.(3). If one of the particles is "green," then they are treated as an external contact-pair and computed by the second term of Eq.(3). The direction of the branch vectors must be carefully determined. In addition, a process needs to handle particle-boundary contacts if it is a boundary process. For example, processes p0-3 are all boundary processes, as shown in Fig.5. The contact force vectors and associated branch vectors accounting for the *boundary-radius-gap* between the boundary surface and its particles must be evaluated properly in order for the stress tensor calculation to be correctly computed.

6. STRESS TENSOR CALCULATION IN SERIAL COMPUTING

Before calculating stress for MPI mode of the 3D DEM code *ParaEllip3d*, serial and OpenMP-enabled numerical simulations are performed to calculate the average stress tensor and quantify its symmetry or lack thereof. The OpenMP-enabled numerical simulations use 16 or 32 cores to accelerate the computation.

ParaEllip3d is a 3D DEM code developed at the University of Colorado Boulder with general capacity to simulate a wide range of laboratory experiments and in-situ field tests that involve a large number of complex-shaped (i.e., non-spherical) particles. The interparticle contact constitutive relation is based on the nonlinear Hertzian normal contact model and history-dependent Mindlin shear contact model, combined with Coulomb friction and interparticle contact damping, which are described in detail and verified numerically in Yan (2008); Yan et al. (2010). The simulated particle shapes range from spherical to three-axis ellipsoidal (with variation of 1st and 2nd aspect ratios), to non-axisymmetric ploy-ellipsoidal (with variation of 1st

and 2nd aspect ratio, and variation of three non-axisymmetry ratios). The simulation types include but are not limited to: grain number/size/mass distribution and filtering; gravitational deposition (pluviation or raining); degravitation response; isotropic compression; oedometer/uniaxial compression; conventional triaxial compression; true triaxial compression; plane-strain compression; quasi-static and dynamic penetration; high-strain-rate impact and deformation; compressive and shear wave propagation; constrained and unconstrained collapse; hierarchical multiscale coupling with FEM; and two-way multiphysics coupling with Computational Fluid Dynamics (CFD) for shock wave or explosive wave interaction. Fundamentals of the DEM such as time integration method, rotation of ellipsoids, contact resolution, energy statistics, etc, are detailed in Yan (2008); Yan et al. (2010); Yan and Regueiro (2018a).

6.1. Damping mechanism

In DEM, two forms of damping mechanism are usually applied: (1) global damping (also referred to as background damping), which operates on the absolute velocities and angular velocities of the particles. Global damping as such may be envisioned as the effect of dashpots connecting each particle to ground (Cundall and Strack, 1979), which is not physically-based; (2) interparticle contact damping is essential and physical to model the mechanical interaction between particles, which is especially true for dynamic problems where interparticle collisions dominate the kinetic energy dissipation. The contact interface is illustrated in Fig.6, characterized by normal stiffness k_n, shear stiffness k_t, friction coefficient μ, and normal contact damping coefficient c_n.

For example, the normal damping coefficient c_n (Onate and Rojek, 2004) can be taken as a fraction of the critical damping C_{cr} for the system of two rigid bodies with masses m_1 and m_2, connected with a spring of stiffness k_n (Taylor and Preece, 1992):

$$C_{cr} = 2\sqrt{\frac{m_1 m_2 k_n}{m_1 + m_2}} \tag{21}$$

$$c_n = \xi C_{cr} \tag{22}$$

where ξ is the damping ratio. Note this damping ratio ξ portrays interparticle energy dissipation and can be calibrated with experiments recorded by high-speed cameras. We found that it ranges between $0.25 \sim 0.85$ by observation

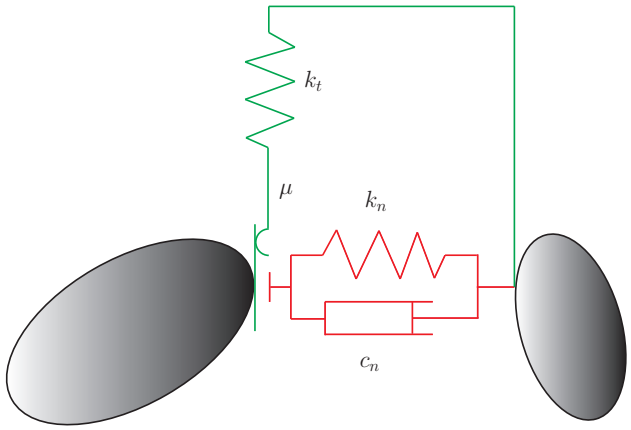

Figure 6: Model of contact interface.

of numerous experimental and numerical tests of pluviation; it is taken as 1.0 in quasi-static simulations. In the shear direction of contact between particles, friction dissipates energy.

The global damping (translational and rotational) is usually applied to each individual particle and unavoidably affects the linear and angular momentum of the particle; the interparticle contact damping (along in-contact normal and shear relative velocity directions) is applied to each pair of in-contact particles as a pair of action and reaction "forces," which has no bearing on the linear momentum, or angular momentum for monodisperse spherical particle assemblies, yet may have slight influence on angular momentum of general particle assemblies. Obviously, the stress tensor formulas presented in this paper do not take this into account. Static simulations or static equilibrium state obtained by dynamic simulations do not have this problem, because the damping mechanism normally vanishes at the instant of reaching static equilibrium.

Note that all simulations in this paper only use interparticle damping, and do not apply any global damping in order to eliminate the influence of damping "force" on the linear and angular momentum of the particle assembly in dynamic or quasi-static state.

Static states of a particle assembly are obtained from gravitational deposition, in which particles are initially "floated" in space without interaction, and then gravitationally-deposited into a rigid container. At the end of the simulation, all particles come to rest and are packed under gravity. The parameters are listed in Table 1. The following sections provide the stress

tensor calculations from Yan and Regueiro (2018d) (in review) for completeness and comparison with later results from parallel computing.

Young's modulus E (Pa)	4.5×10^{10}
Poisson's ratio ν	0.25
specific gravity G_s	2.65
interparticle coef. of friction μ_1	0.5
particle-wall coef. of friction μ_2	0.5
interparticle contact damping ratio ξ	$0.25 \sim 0.85$
particle radii (m)	$0.001 \sim 0.0025$
particle shape (aspect ratio)	1:1:1, 1:0.8:0.6, 1:0.8:0.4, 1:0.6:0.4
time step $\triangle t$ (sec)	5.0×10^{-7} or smaller

Table 1: Numerical parameters used in gravitational pluviation simulations.

6.2. Monodisperse spherical particle assemblies

Monodisperse spherical particle (1.5 mm radius) assemblies are simulated with different number of particles: 68, 153, 600, 1,176, 1,536, 2,400 and 3,456, respectively. The final rested state for each of the particle assemblies is illustrated in Fig.7. The processes of boundary contact forces and assembly energy for 68 and 3,456 particles are plotted in Fig.8, and it is observed that the rotational energy contributes a very small fraction relative to the translational energy during the process of particle packing and rebounding.

Table 2 lists the 3x3 matrix of stress tensor components calculated by Weber's and Bagi's formulas for the 7 cases. It is clear that the stress tensor calculated by Weber's formula is asymmetric for small numbers of particles, and the asymmetry decreases with an increasing number of particles. On the other hand, the stress tensor calculated by Bagi's formula exhibits excellent symmetry for all cases (68 particles to 3,456 particles). Even for 3,456 particles, the stress gap between Weber's and Bagi's formulas is still apparent. The RAI's are calculated for all cases. By Weber's formula, it is as high as 15.1% for 68 particles and as low as 1.1% for 1,176 particles, while it is below 0.03% by Bagi's formula for all cases. As a technical index, a RAI value of 1% indicates clear asymmetry, and 5% represents strong asymmetry.

6.3. Polydisperse ellipsoidal particle assemblies

Polydisperse ellipsoidal particle assemblies (1.0 to 2.5 mm radius) are simulated with different number of particles: 69, 179, 476, 1,071, 1,904 and

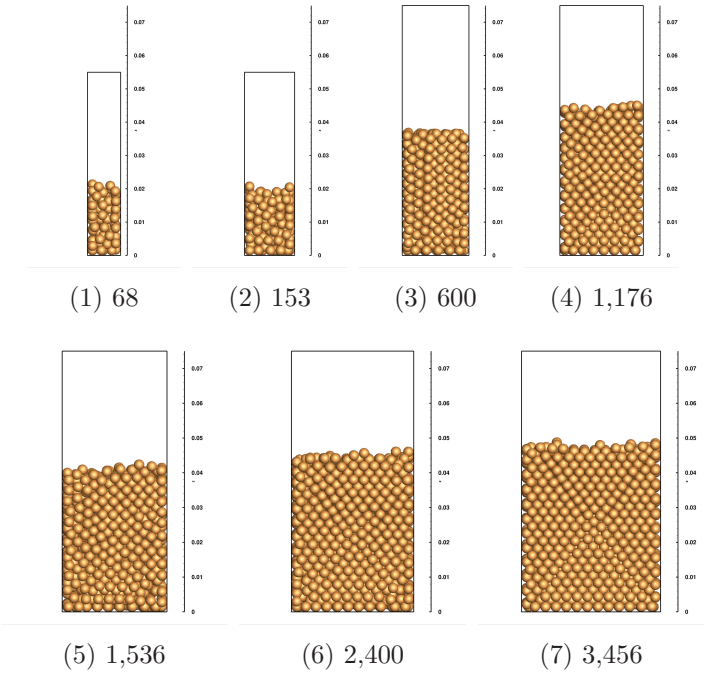

(1) 68 (2) 153 (3) 600 (4) 1,176

(5) 1,536 (6) 2,400 (7) 3,456

Figure 7: Rested state of monodisperse spherical particle assemblies.

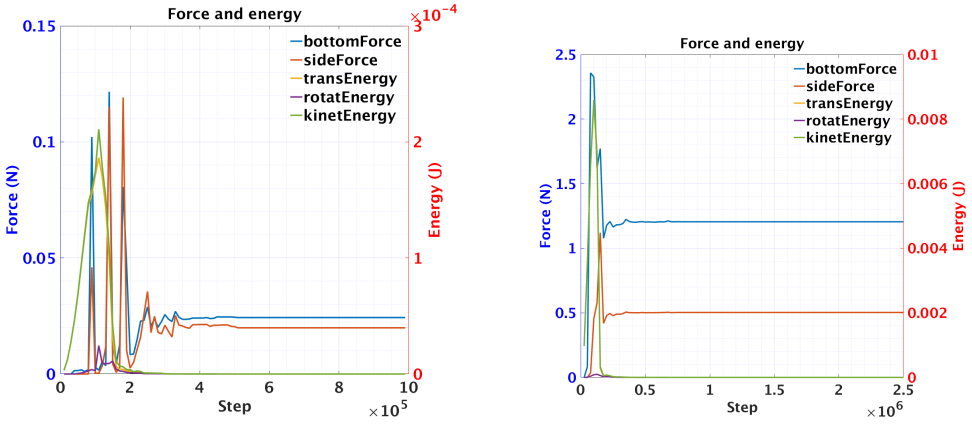

(a) 68 particles (b) 3,456 particles

Figure 8: Boundary contact forces and assembly energy in gravitational deposition.

Table 2: Static stress tensor of monodisperse spherical particle assemblies.

particles	Weber's formula stress tensor			RAI (%)	Bagi's formula stress tensor			RAI (%)
	-6.44E+01	-1.15E+01	-2.72E+00		-9.07E+01	-9.70E+00	-1.19E+00	
68	-8.11E+00	-6.16E+01	-5.34E+00	15.1	-9.70E+00	-8.76E+01	-4.44E+00	8.03E-05
	-1.37E+00	-5.50E+00	-1.09E+02		-1.19E+00	-4.44E+00	-1.25E+02	
	-8.12E+01	-2.31E-01	2.55E+00		-1.01E+02	4.87E-01	2.82E+00	
153	-1.35E-04	-7.86E+01	-8.39E+00	2.2	4.87E-01	-9.84E+01	-9.15E+00	2.33E-03
	2.54E+00	-8.09E+00	-9.68E+01		2.82E+00	-9.15E+00	-1.15E+02	
	-1.46E+02	-2.85E+01	8.86E+00		-1.71E+02	-2.83E+01	7.75E+00	
600	-2.72E+01	-1.51E+02	1.48E+01	2.2	-2.83E+01	-1.76E+02	1.50E+01	5.29E-05
	9.21E+00	1.56E+01	-2.54E+02		7.75E+00	1.50E+01	-2.80E+02	
	-2.35E+02	3.97E+01	-8.45E+00		-2.66E+02	3.95E+01	-8.25E+00	
1,176	3.96E+01	-2.34E+02	-1.42E+01	1.1	3.95E+01	-2.65E+02	-1.39E+01	1.74E-05
	-7.88E+00	-1.34E+01	-3.05E+02		-8.25E+00	-1.39E+01	-3.27E+02	
	-1.88E+02	-9.42E+00	4.69E+00		-2.09E+02	-9.84E+00	5.25E+00	
1,536	-9.95E+00	-1.90E+02	-1.05E+00	5.2	-9.84E+00	-2.11E+02	-4.00E-01	2.71E-02
	5.62E+00	-5.35E-01	-2.55E+02		5.25E+00	-4.00E-01	-2.76E+02	
	-2.42E+02	-3.77E+00	-8.39E+00		-2.65E+02	-3.84E+00	-8.16E+00	
2,400	-4.24E+00	-2.43E+02	2.18E+00	4.0	-3.84E+00	-2.66E+02	2.56E+00	2.94E-04
	-8.16E+00	2.81E+00	-3.32E+02		-8.16E+00	2.56E+00	-3.55E+02	
	-2.29E+02	1.11E+01	-2.17E+00		-2.47E+02	1.10E+01	-1.98E+00	
3,456	1.14E+01	-2.29E+02	-1.89E+00	1.7	1.10E+01	-2.48E+02	-1.64E+00	2.07E-03
	-2.07E+00	-1.57E+00	-3.56E+02		-1.98E+00	-1.64E+00	-3.79E+02	

2,975, respectively. The final rested state of each of the particle assemblies is illustrated in Fig.9.

Table 3 lists the 3x3 matrix of stress tensor components calculated by Weber's and Bagi's formulas for the 6 cases. It exhibits a trend similar to that for monodisperse spherical particle assemblies. The stress from Bagi's formula exhibits excellent symmetry. Note that contact geometry resolution between ellipsoids is numerically challenging. As an estimate, modern supercomputers are typically capable of computing up to $15,000 \sim 30,000$ particles per core (PPC) of spheres, and $150 \sim 300$ PPC of complex-shaped particles such as ellipsoids or poly-ellipsoids with optimal computational granularity (CG) for large-scale MPI simulations (Yan and Regueiro, 2018b). The RAI by Weber's formula ranges from 3.9% to 30.0%, indicating strong asymmetry; while it is typically below 0.3% calculated by Bagi's formula for all cases.

It was proven in Section 3 that the Cauchy stress tensor is symmetric under static conditions for CCM and GMM. Bardet and Vardoulakis (2001) stated that computed stress tensor asymmetry implies inaccurate calculation and/or lack of static equilibrium. The simulations of different shapes and size gradation of particles in this section provide clear numerical verification that at rested (static) state, Bagi's formula provides a symmetric stress tensor, whereas Weber's formula does not. We emphasize that stress tensor sym-

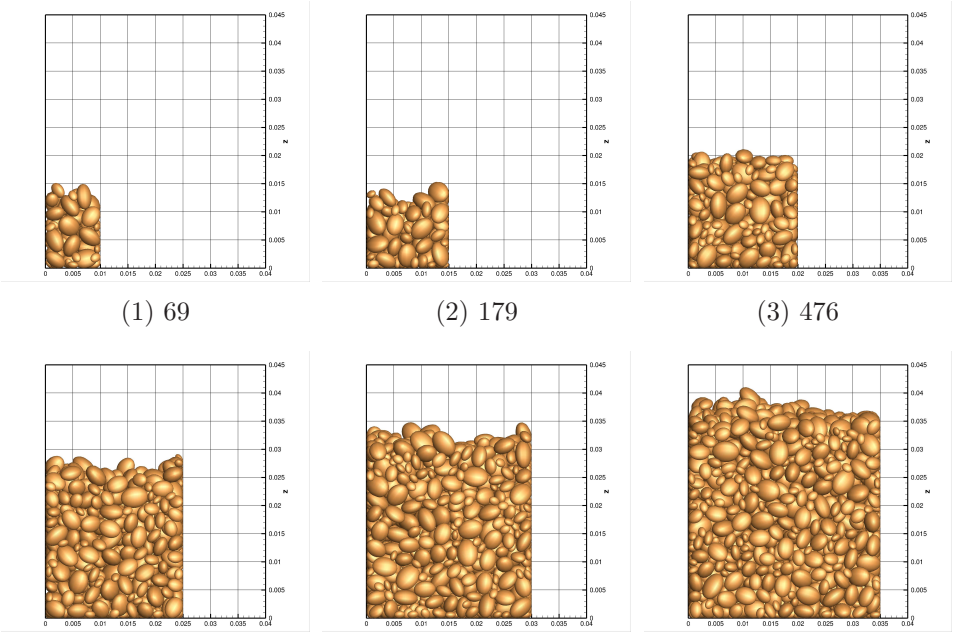

(1) 69 (2) 179 (3) 476

(4) 1,071 (5) 1,904 (6) 2,975

Figure 9: Rested state of polydisperse ellipsoidal particle assemblies.

Table 3: Static stress tensor of polydisperse ellipsoidal particle assemblies.

particles	Weber's formula stress tensor			RAI (%)	Bagi's formula stress tensor			RAI (%)
	-2.83E+01	1.76E+00	9.77E-02		-4.12E+01	-5.52E-01	1.77E+00	
69	1.39E+00	-3.77E+01	1.30E+01	3.9	-6.30E-01	-5.75E+01	1.57E+01	2.80E-01
	-3.45E-01	1.39E+01	-6.30E+01		1.74E+00	1.57E+01	-8.10E+01	
	-4.62E+01	5.09E-01	3.03E-01		-5.81E+01	7.73E-01	9.67E-01	
179	1.44E+00	-4.10E+01	2.27E+00	30.0	7.73E-01	-5.09E+01	8.39E-01	2.47E-03
	-4.20E-01	1.66E+00	-5.61E+01		9.67E-01	8.39E-01	-6.98E+01	
	-8.36E+01	5.66E+00	1.58E+00		-9.81E+01	3.67E+00	1.57E+00	
476	3.58E+00	-8.39E+01	2.35E+00	20.3	3.67E+00	-9.74E+01	2.62E+00	3.29E-03
	1.90E+00	3.94E+00	-1.09E+02		1.57E+00	2.62E+00	-1.26E+02	
	-1.19E+02	7.53E+00	2.66E+00		-1.36E+02	8.36E+00	3.67E+00	
1,071	6.95E+00	-1.18E+02	3.81E-01	6.3	8.36E+00	-1.33E+02	-3.01E-01	9.05E-03
	3.41E+00	7.62E-01	-1.51E+02		3.68E+00	-3.00E-01	-1.66E+02	
	-1.32E+02	-2.81E+00	8.30E+00		-1.47E+02	-1.49E+00	9.85E+00	
1,904	-2.27E+00	-1.29E+02	-7.09E-02	4.8	-1.49E+00	-1.43E+02	-8.66E-01	2.23E-02
	8.36E+00	-7.34E-01	-1.79E+02		9.85E+00	-8.62E-01	-1.96E+02	
	-1.60E+02	1.49E+00	-5.74E-01		-1.75E+02	1.25E+00	5.09E-01	
2,975	1.09E+00	-1.71E+02	3.43E+00	6.3	1.24E+00	-1.85E+02	4.35E+00	2.37E-02
	-1.00E-01	3.80E+00	-2.13E+02		5.07E-01	4.35E+00	-2.29E+02	

metry is independent of the RVE size, or size of averaging volume, which is contrary to the conclusion by Lin and Wu (2016). In addition, from the perspective of stress tensor calculation, the number of particles in the RVE does not need to be large, namely, tens or hundreds of particles would be adequate provided that high-precision contact geometric resolution is assured, which *ParaEllip3d* successfully provides.

6.4. Bagi's vs Weber's vs Drescher's formulas

The static stress tensor calculated from Weber's, Drescher's, and Bagi's formulas are compared in Table 4, using the assembly of 1,536 monodisperse spherical particles.

Table 4: Stress tensors calculated from various formulas

formula	stress tensor			RAI (%)
Bagi	-2.09E+02	-9.84E+00	5.25E+00	0.028
	-9.84E+00	-2.11E+02	-4.00E-01	
	5.25E+00	-4.00E-01	-2.76E+02	
Weber	-1.88E+02	-9.42E+00	4.69E+00	5.2
	-9.95E+00	-1.90E+02	-1.05E+00	
	5.62E+00	-5.35E-01	-2.55E+02	
Drescher	-2.09E+02	-9.84E+00	5.25E+00	94.7
	-9.84E+00	-2.11E+02	-4.74E-01	
	2.19E+02	2.14E+02	1.88E+01	

First, the stresses calculated by Weber's and Drescher's formulas are asymmetric and are different from the result of Bagi's formula. Second, the RAI by Bagi's formula is low (below 0.03%), whereas the RAI by Weber's formula is 5.2% indicating strong asymmetry, and the RAI by Drescher's formula is 94.7% representing high asymmetry. In addition, the σ_{zz} (or σ_{33}) component by Drescher's formula deviates significantly from that by Weber's and Bagi's formulas.

7. STRESS TENSOR CALCULATION IN PARALLEL COMPUTING

7.1. DoD supercomputers

The target architectures in this work are four of the DoD supercomputers: Thunder, Topaz, Excalibur, and Onyx, and their architectural parameters are listed in Table 5.

Table 5: Four DoD Supercomputers (`https://centers.hpc.mil/systems/summary.html`).

supercomputer	Thunder	Topaz	Excalibur	Onyx
system	SGI ICE X	SGI ICE X	Cray XC40	Cray XC40/50
compute nodes	3,576	3,492	3,162	3,438
cores per node	36	36	32	44
total cores	125,888	125,440	101,184	161,448
memory per node	128 GB	128 GB	128 GB	128 GB
CPU	Xeon E5-2699v3	Xeon E5-2699v3	Xeon E5-2698v3	Xeon E5-2699v4
core speed	2.3 GHz	2.3 GHz	2.3 GHz	2.8 Ghz
interconnect	4x FDR InfiniBand	4x FDR InfiniBand	Cray Aries	Cray Aries
peak PFLOPS	5.62	4.66	3.77	6.06
default MPI	SGI MPT	SGI MPT	Cray MPICH2	Cray MPICH2

7.2. Stress tensor symmetry

A parallel simulation depositing 7,200 spherical particles into a rigid container is conducted using 3 x 3 x 4 compute grids in x, y, z directions, respectively, as illustrated in Fig.4. Spatial distribution of σ_{zz} in the rested state is plotted in Fig.10. Note that some of the digits are hidden due to post-process rendering effect, and only the numbers at the top and left parts of the figure are readable.

Stress tensors over the grids are calculated in the rested state using Bagi's formula. From nine columns of compute grids, the central column and an edge column are selected to print out their stress tensor values in top-down order in Table 6. It is seen that excellent symmetry is achieved, whether from internal compute grids or from boundary compute grids. This verifies that the stress tensor calculation algorithm in MPI parallel 3D DEM is implemented correctly. It is also observed that σ_{zz} increases with depth due to gravity, as expected.

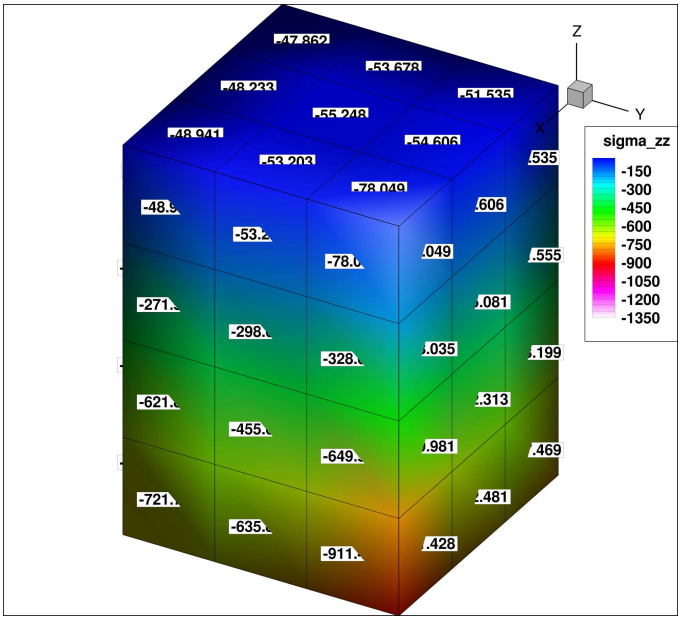

Figure 10: σ_{zz} distribution of 7,200 particles using 3 x 3 x 4 grids.

Table 6: Static stress tensors calculated over parallel computing grids.

grid	central column stress tensor			RAI (%)	edge column stress tensor			RAI (%)
	-4.17E+01	-4.81E+00	-2.16E+00		-6.17E+01	3.89E-01	-8.70E+00	
top	-4.81E+00	-4.17E+01	-2.95E+00	2.68E-02	3.89E-01	-6.50E+01	-1.03E+01	5.32E-04
	-2.16E+00	-2.94E+00	-5.52E+01		-8.70E+00	-1.03E+01	-7.80E+01	
	-3.99E+02	-1.55E+01	-5.02E+00		-2.77E+02	-2.55E+01	9.72E+00	
mid-top	-1.55E+01	-3.89E+02	-2.18E+00	1.50E-03	-2.55E+01	-3.27E+02	-4.63E+01	1.32E-04
	-5.02E+00	-2.18E+00	-4.74E+02		9.72E+00	-4.63E+01	-3.28E+02	
	-6.31E+02	-1.10E+02	-2.17E+01		-4.32E+02	-1.51E+02	1.00E+02	
mid-bottom	-1.10E+02	-5.97E+02	-1.14E+01	3.56E-04	-1.51E+02	-4.09E+02	1.30E+02	2.77E-05
	-2.17E+01	-1.14E+01	-1.06E+03		1.00E+02	1.30E+02	-6.50E+02	
	-7.29E+02	-1.93E+01	-4.93E-01		-5.63E+02	-1.51E+02	-3.12E+01	
bottom	-1.93E+01	-7.19E+02	7.80E+00	2.29E-04	-1.51E+02	-5.67E+02	-2.02E+01	5.41E-04
	-4.93E-01	7.80E+00	-1.38E+03		-3.12E+01	-2.02E+01	-9.11E+02	

7.3. Spatial distribution of σ_{zz}

Three different spherical particle assemblies (7k, 50k, and 250k particles, respectively) are used to investigate the spatial distribution of σ_{zz} utilizing parallel computing. The particles are dropped into rigid containers via gravitational pluviation, and then the assemblies are trimmed flat at the top surface. High-resolution movies generated from the simulations of gravitational deposition are displayed at the following YouTube playlist (note: play with 1080p or 1440p HD option to observe details): https://www.youtube.com/playlist?list=PL0Spd0Mtb6vXWB2qqR0k6Hc35Qcj12tXr

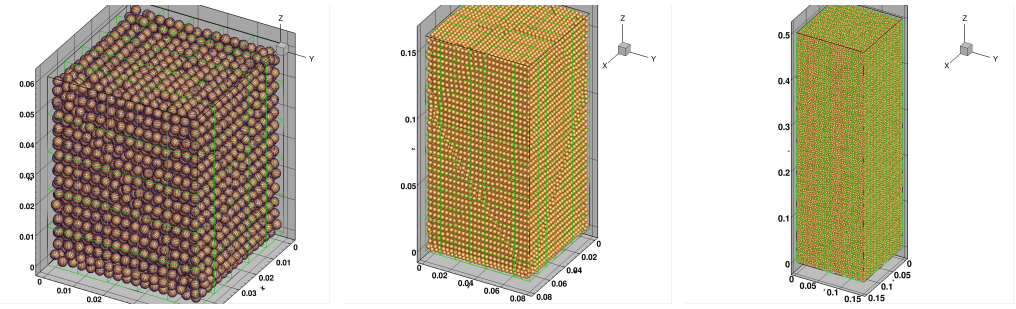

(a) 7k particles. (b) 50k particles. (c) 250k particles.

Figure 11: Top-trimmed spherical particle assemblies.

The top-trimmed assemblies consist of 7k, 50k, and 250k particles, respectively, and their heights are 0.06 cm, 0.15 cm, and 0.50 cm, respectively, as shown in Fig.11. The number of particles per grid in parallel computing is roughly 55, 75, and 55 for the three specimens, respectively. A vertical slice view of σ_{zz} is plotted for the three assemblies in Fig.12, wherein the σ_{zz} contours exhibit a dome-shaped spatial distribution. Zebra-shaded graphs are used to plot the distribution more clearly in Fig.13, exhibiting σ_{zz} contour dome-shapes for each of the three different assemblies. The spatial distribution captured by parallel computing of 3D DEM differs from that calculated by CCM, which would provide evenly-distributed σ_{zz} in the horizontal direction for the case of no boundary friction, as shown later in Fig.27(b).

The dome-shaped spatial distribution of σ_{zz} is associated with conducting pluviation in a relatively narrow container, which prevents particles from moving laterally, locking up different microstructures along horizontal levels. As illustrated later in Section 9.2, the horizontal stress σ_{yy} also produces a dome-shaped distribution. From the vertical centerline to side walls of the

container, the lockup may become more pronounced and result in such stress distributions. This conjecture will be further studied by analysis of internal topology and fabric across the particle assemblies, for example, using *Qhull* (www.qhull.org), which enables construction of tetrahedra in 3D space that connect the centroids of every four neighboring particles, or the contact points of every four neighboring interparticle contact pairs, and examines important geometric quantities such as tetrahedral shape/volume, solid angles, dihedral angles, etc.

In addition, Section 9.2 delineates incremental displacement (Fig.26) and dislocation pattern (Fig.29) of the particle assemblies as a result of pluviation, which could also contribute to the stress distribution.

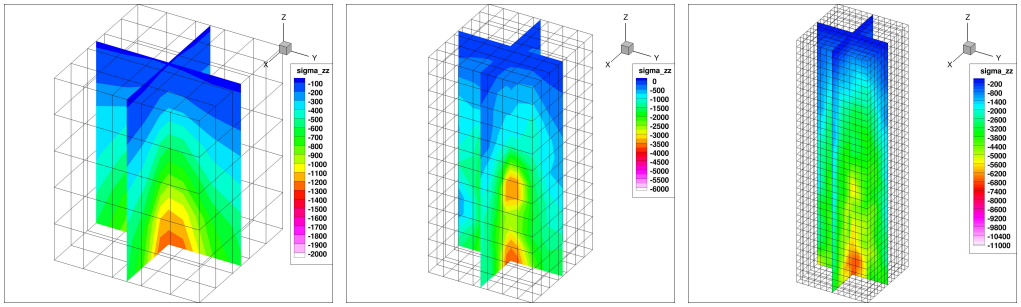

(a) 7k particles. (b) 50k particles. (c) 250k particles.

Figure 12: Vertical slice view of σ_{zz}.

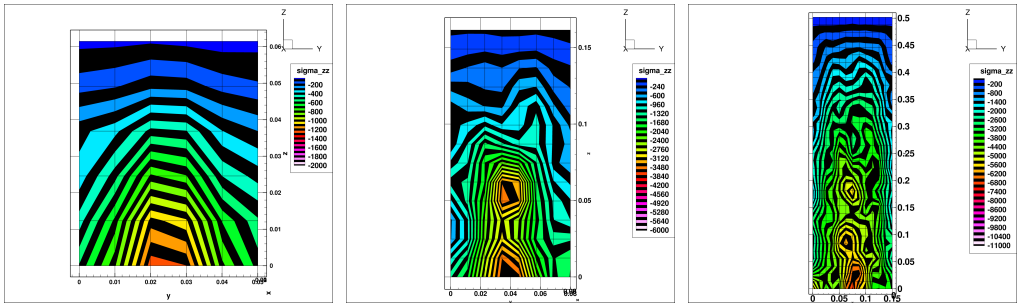

(a) 7k particles. (b) 50k particles. (c) 250k particles.

Figure 13: Vertical slice view of σ_{zz}.

Figure 14 provides a horizontal slice view of σ_{zz} for the three assemblies. In the center, a ring-shaped distribution is revealed. An isosurface view of σ_{zz} is presented in Fig.15: (a) side view of the 7k particle assembly, where

the dome-shape is plotted by an isosurface; and (b) bottom view of the 250k particle assembly.

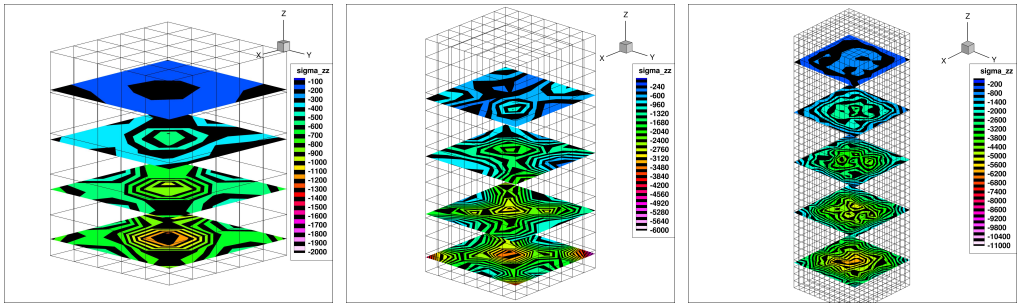

(a) 7k particles. (b) 50k particles. (c) 250k particles.

Figure 14: Horizontal slice view of σ_{zz}.

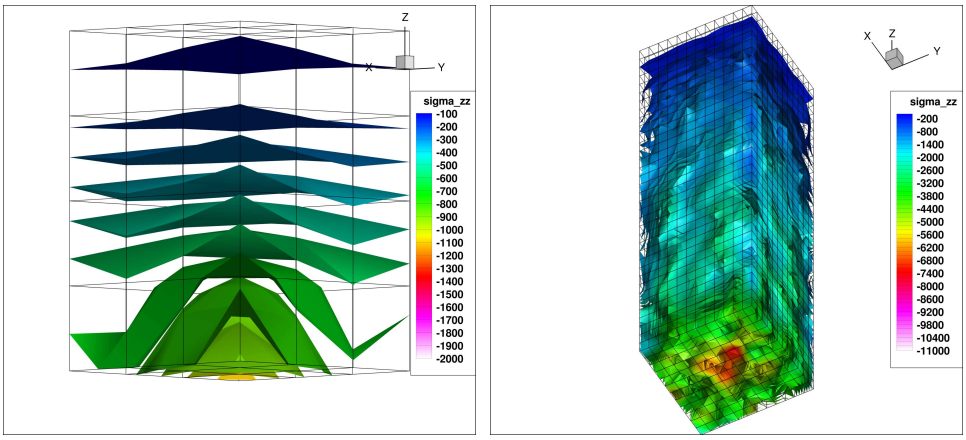

(a) 7k particles. (b) 250k particles.

Figure 15: Isosurface view of σ_{zz} for 7k and 250k assemblies.

7.4. Influence of compute grid sizes

For each of the seven equations that calculate stress in granular materials, Eq.(1)∼(7), the term V denotes volume of the RVE. In parallel computing of 3D DEM, V is dependent on the size of the compute grids. It is interesting to recognize that the dynamically-adaptive compute grids used in MPI parallel 3D DEM are neither purely Lagrangian nor purely Eulerian: (a) the compute grids provide spatial domain decomposition for parallel computing

and are not tied to particles, though they follow the overall motion of the particle assembly in 3D space, similar to a Lagrangian perspective; and (b) generally the compute grids are not Eulerian; however, they become Eulerian if they are fixed on purpose, which provides a flexible way to observe fluid-like behavior of granular materials (but adversely affects load balancing in parallel computing).

Figure 16 displays σ_{zz} along the compute grid surfaces of the 50k particle assembly at rest using 3x3x5, 5x5x7, and 7x7x13 grids (1110, 285, 78 particles per grid accordingly), respectively. Apparently different values are presented at the same location. For example, the center grid on the left-front surface provides -933, -1111, and -987 Pa for σ_{zz} for the three different grids, respectively. Overall, denser grids produce higher σ_{zz} at greater depth and produce lower σ_{zz} at lower depth due to volume averaging effect.

Table 7 lists the stress tensor components calculated in the center compute grid of 7k and 50k particle assemblies, respectively, using different combinations of grids. The normal stress components increase with denser grids (i.e., smaller grid sizes) in the case of 7k particles, and decrease with denser grids in the case of 50k particles. In general, the magnitude of stress tensor components does not have a monotonic relation with the averaging volume used to calculate the stress tensor, and it actually depends on the spatial location of the grid inside the particle assembly. Furthermore, the size of the compute grids in parallel computing can be flexibly chosen, according to a particular length-scale effect of interest to be resolved by the analyst.

Table 7: Stress tensor calculated using different compute grids

grids	center grid of 7k particles stress tensor			grids	center grid of 50k particles stress tensor		
	-3.20E+02	-5.98E+00	-4.02E+00		-1.12E+03	-6.30E+00	-1.87E+02
1x1x1	-5.98E+00	-3.18E+02	-8.32E+00	3x3x5	-6.30E+00	-1.08E+03	-1.11E+02
	-4.02E+00	-8.32E+00	-4.68E+02		-1.87E+02	-1.11E+02	-1.87E+03
	-5.09E+02	-1.11E+02	-2.19E+01		-7.42E+02	-1.20E+02	-3.81E+02
3x3x3	-1.11E+02	-5.00E+02	-1.83E+01	5x5x9	-1.20E+02	-6.98E+02	-3.32E+02
	-2.19E+01	-1.83E+01	-8.01E+02		-3.81E+02	-3.32E+02	-1.26E+03
	-5.25E+02	-9.91E+01	-1.50E+02		-4.92E+02	-1.23E+02	-2.97E+02
5x5x5	-9.91E+01	-4.73E+02	-9.51E+01	7x7x13	-1.23E+02	-4.46E+02	-2.27E+02
	-1.50E+02	-9.51E+01	-1.18E+03		-2.97E+02	-2.27E+02	-8.07E+02

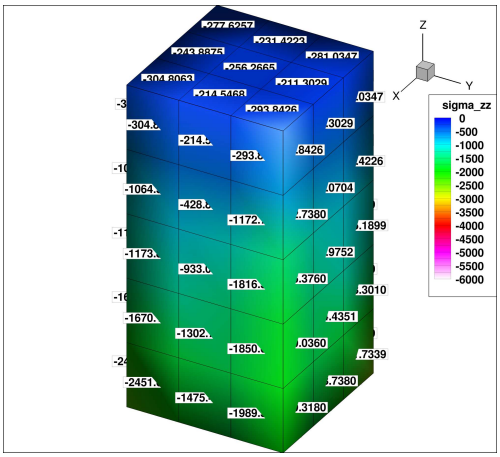

(a) 3x3x5 grids.

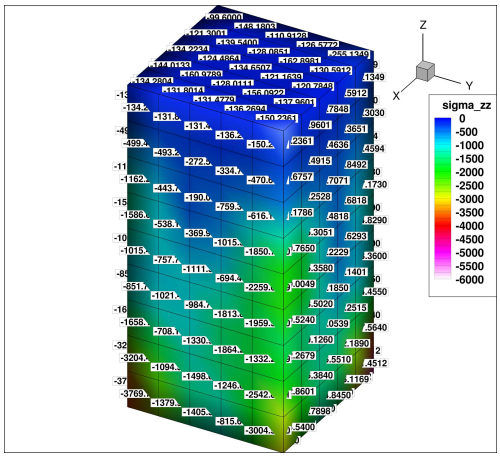

(b) 5x5x9 grids.

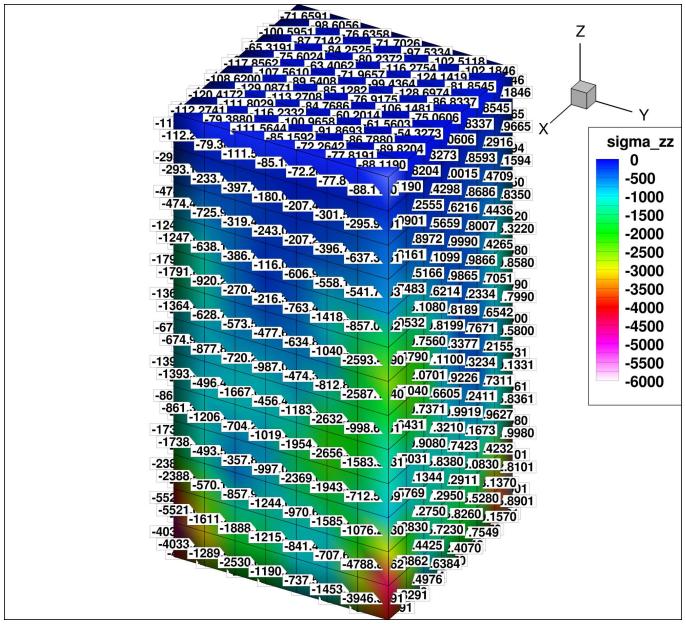

(c) 7x7x13 grids.

Figure 16: 3D view of σ_{zz} using different compute grids (zoom-in to the PDF file to see the small-font numbers).

8. STRESS DISTRIBUTION DURING DYNAMIC PROCESSES

8.1. Gravitational pluviation

The temporal and spatial distributions of σ_{zz} during gravitational pluviation are studied using the third particle assembly described in Section 7.3. The specimen consists of 250k particles that are initially floated up to 1.5 meters in height, and then allowed to drop under gravity into a rigid container. Each parallel computing grid contains roughly 55 particles. The contour plots of vertical stress σ_{zz} are shown in two movies at YouTube:

- σ_{zz}: https://youtu.be/OtZoVFKRHjg
- zoomed-in σ_{zz}: https://youtu.be/FBG4HQK4Hzo

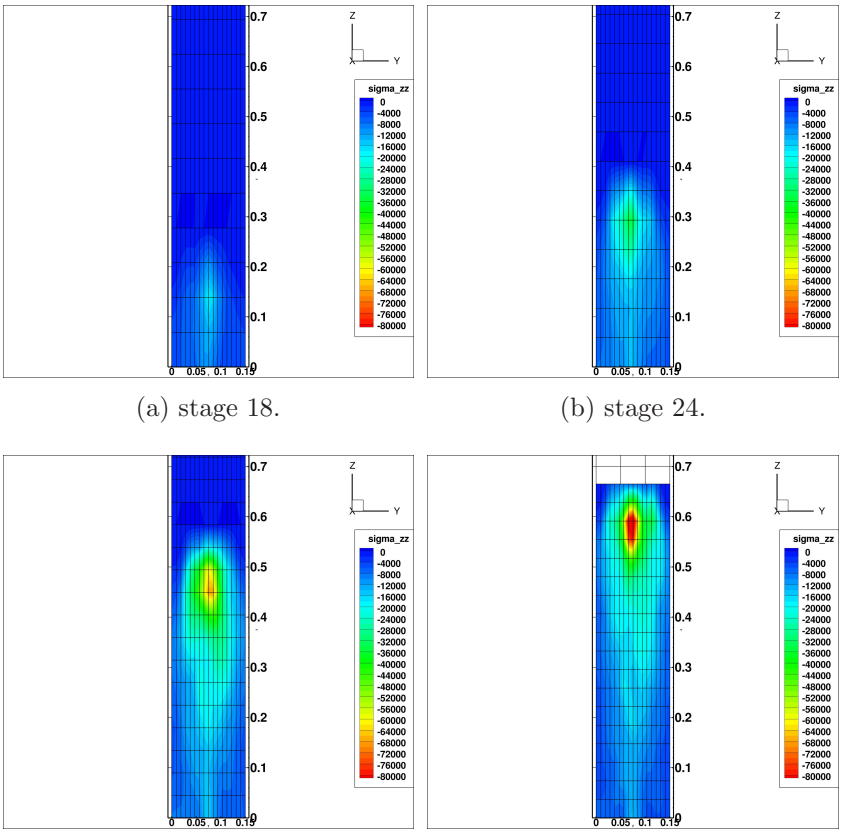

(a) stage 18. (b) stage 24.

(c) stage 30. (d) stage 33.

Figure 17: σ_{zz} at different stages of 250k particle pluviation.

The simulation output is evenly divided into 100 stages in time, and Fig.17 displays σ_{zz} contour distributions at stages 18, 24, 30 and 33, respectively. Note that blue color indicates zero stress. During pluviation, as the particles start to pack at the bottom of the container, the location of maximum σ_{zz} keeps moving up until all particles are packed. When comparing the following two movies:

- particles: https://youtu.be/V23MyTCdEGg
- σ_{zz}: https://youtu.be/FBG4HQK4Hzo,

it is seen that the location of maximum σ_{zz} is near the top surface of the packed particles, where the most intense collisions occur between particles. Figure 18 shows the σ_{zz} contour distribution and particle assembly state at stage 30, side-by-side for easier comparison.

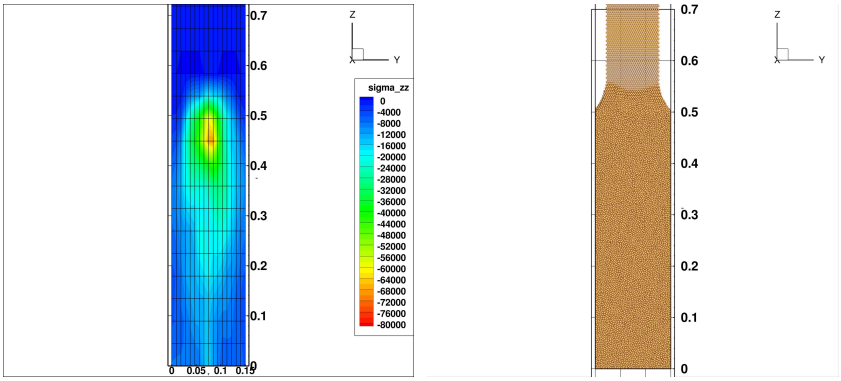

(a) σ_{zz}. (b) particles.

Figure 18: σ_{zz} vs particle assembly state at stage 30.

8.2. Constrained collapse

Numerical collapse simulations using 535k different-shaped particles are performed to observe stress tensor component distributions. The simulation process is essentially the same as pluviation, but using a wider container (and more particles) to observe the collapse and expansion of the particle assemblies. Each parallel computing grid contains roughly 60 particles. Four particle shapes are chosen with the following aspect ratios: sphere (1:1:1), ellipsoid-1 (1:0.8:0.6), ellipsoid-2 (1:0.8:0.4), and ellipsoid-3 (1:0.6:0.4), of which the maximum particle semi-axis length is 2 mm. 3D details of the particle motion can be watched via the following movies at YouTube:

- sphere: https://youtu.be/ZVX4-fREy2M
- ellipsoid-1: https://youtu.be/nrUUp1rz9OY
- ellipsoid-2: https://youtu.be/AQuG2tKeZC4
- ellipsoid-3: https://youtu.be/6XuyaMCjpll

Figure 19 demonstrates the collapse of 535k particles with 8 snapshots in time. Note the scattered particles in the central area of Fig.19 ($4 \sim 6$) that are rebounded from the front/back walls, not from the left/right walls. Figure 20 shows the cross-sectional view of sphere and ellipsoid-1 assemblies at rest.

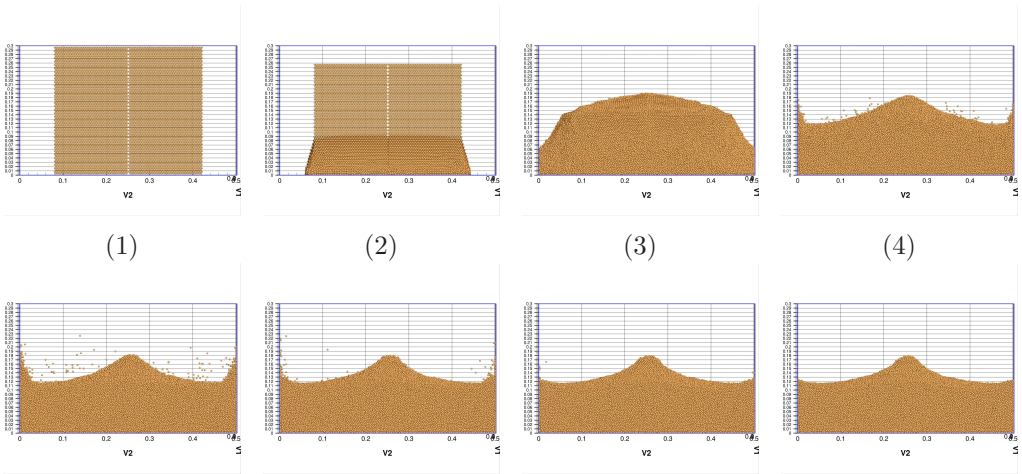

(1) (2) (3) (4)

(5) (6) (7) (8)

Figure 19: Side view of the collapse process of 535k particles.

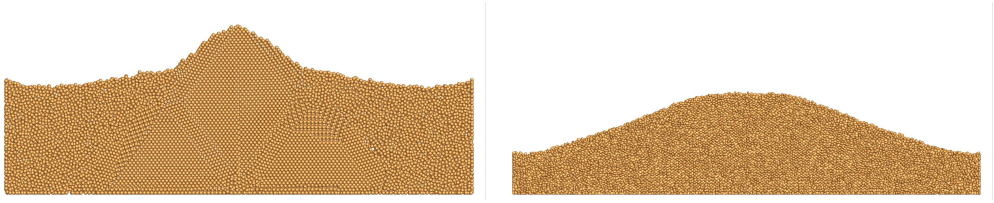

(a) Sphere. (b) Ellipsoid-1.

Figure 20: Cross-sectional view of sphere and ellipsoid-1 assemblies at rest.

Detailed temporal and spatial distributions of σ_{zz} can be viewed via the following movies at YouTube:

- sphere σ_{zz}: https://youtu.be/JevBgyBnLJA
- ellipsoid-1 σ_{zz}: https://youtu.be/0SaBOo57mqY
- ellipsoid-2 σ_{zz}: https://youtu.be/RY6gh2xazis
- ellipsoid-3 σ_{zz}: https://youtu.be/ZBNBo1p-PEg

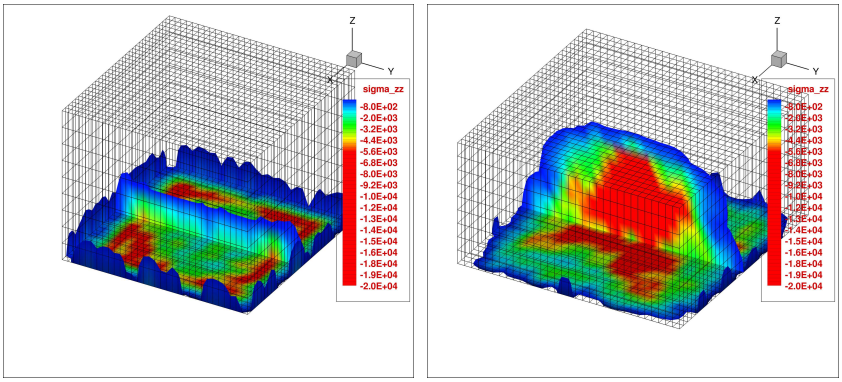

(a) stage 04. (b) stage 08.

(c) stage 12. (d) stage 40.

Figure 21: σ_{zz} contours at different stages of 535k particle collapse.

The collapse simulation output is also evenly divided into 100 stages in time, and Fig.21 displays the σ_{zz} contours for the sphere assembly at stages 04, 08, 12, and 40, respectively. The stress is plotted using a combination of midplane slice view and boundary view. At stage 04, the bottom of the particle assembly undergoes maximum stress due to particle-wall collision; at stage 08, the collision between upper and lower particles causes the maximum stress; at stage 12, the fluid-like "wave" spreads and hits the side walls of

the container where the maximum stress occurs; and at stage 40, the particle assembly is close to rested/static state.

Figure 22 displays the midplane slice view of σ_{zz} contours at rest using zebra-shaded graphs for the four assemblies with different particle shapes. Overall, a layered stress distribution pattern is observed, parallel to the surface profile of the collapsed particle assemblies.

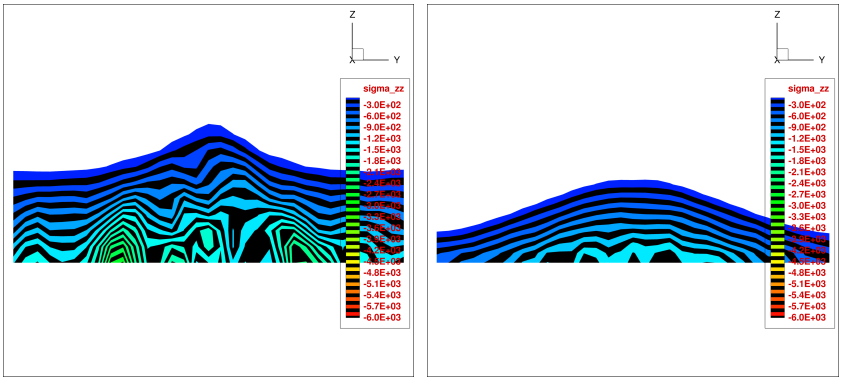

(a) sphere. (b) ellipsoid-1.

(c) ellipsoid-2. (d) ellipsoid-3.

Figure 22: σ_{zz} contours for particles with different aspect ratio.

In contrast to the dome-shaped σ_{zz} contour inside a narrow vertical container, as shown in Section 7.3, the wider container allows more lateral motion of the particles and alleviates the lockup effect along its side walls, resulting in a more evenly-distributed stress contour, particularly in Fig.22(d).

9. MICROSTRUCTURAL EFFECT ON STRESS DISTRIBUTION IN GRANULAR MATERIALS

9.1. Influence of bottom impact in pluviation

In the pluviation simulations, the initial locations of the particles are lifted by a certain distance such that they generate stronger collisions at the bottom of the rigid container. The 7k, 50k, and 250k particle assemblies are lifted by 5, 10, and 20 cm, respectively, to create bottom gaps. The pluviation processes are displayed at the following YouTube playlist: https://www.youtube.com/playlist?list=PL0Spd0Mtb6vVnYZ795H3ku8C-0tBPIPfS.

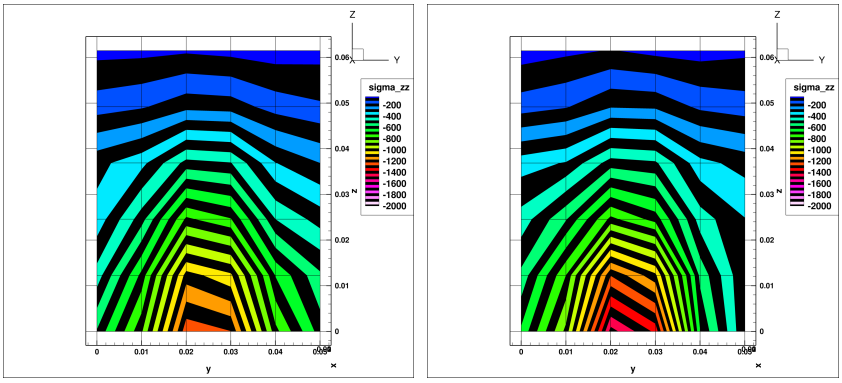

(a) without bottom gap. (b) with 5 cm bottom gap.

Figure 23: σ_{zz} with or without initial bottom gap for 7k particles.

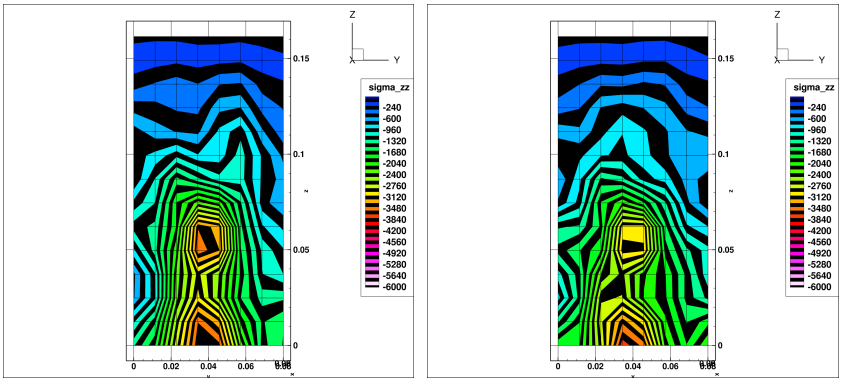

(a) without bottom gap. (b) with 10 cm bottom gap.

Figure 24: σ_{zz} with or without initial bottom gap for 50k particles.

Figure 23 displays the σ_{zz} contours at rest for 7k particles with and without 5 cm bottom gap, for which a slight difference can be noticed; yet, the overall contour distributions are similar. Figure 24 displays the σ_{zz} contours at rest for 50k particles with and without the 10 cm bottom gap. Figure 25 displays the σ_{zz} contours at rest for 250k particles with and without the 20 cm bottom gap. Again, the overall contour distributions are similar, though a slight difference is noticeable. Further investigation into the relations between various pluviation heights and granular material properties such as packing density/void ratio, fabric anisotropy, stress distribution, etc, is needed to better understand the effects.

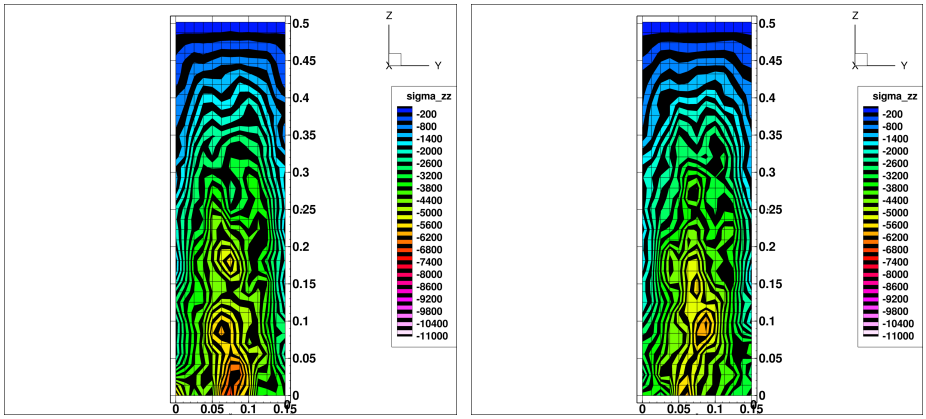

(a) without bottom gap. (b) with 20 cm bottom gap.

Figure 25: σ_{zz} with or without initial bottom gap for 250k particles.

9.2. Influence of friction

Two more cases are investigated for the gravitational pluviation tests: (1) no particle-to-wall friction; (2) no friction whatsoever, i.e., particle-to-particle and particle-to-boundary friction vanish. The particle assembly motions and corresponding incremental displacement vector fields can be observed in the following YouTube playlist: https://www.youtube.com/playlist?list=PL0Spd0Mtb6vVy7jG_XipIqvbejNGtLxa9, wherein six movies play continuously to show the differences. With boundary friction, the deposited/packed particles are locked immediately by the walls; whereas, without boundary friction the deposited/packed particles exhibit a stronger rebound-and-repack process, during which particles clearly slide along the

side and bottom walls. Without friction, the deposited/packed particles exhibit slippage along walls and dislocations between particles.

Figure 26 displays the incremental displacement vector fields at a later stage of the particle assembly motion for the 3 cases, and they exhibit some differences.

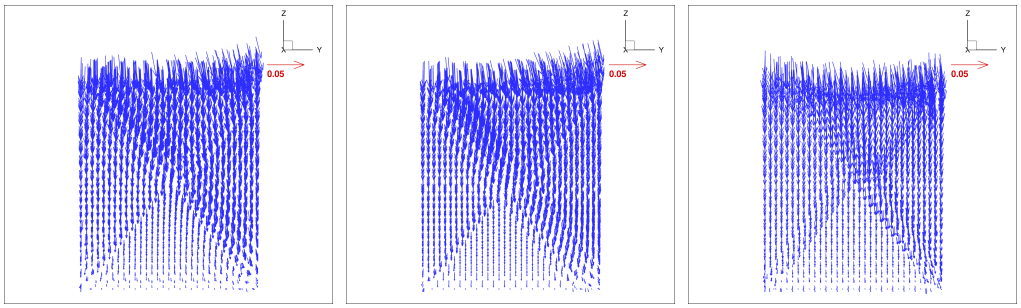

(a) friction. (b) no wall friction. (c) no friction.

Figure 26: Friction effect on incremental displacement vector fields of 7k particle assembly.

Figure 27 displays a slice view of σ_{zz} for the 3 cases. If comparing (a) friction to (b) no wall friction, the difference can be observed in the lower-right zone, although the overall distributions are similar. On the other hand, case (c) provides a noticeably different stress distribution since it represents a different material with zero friction.

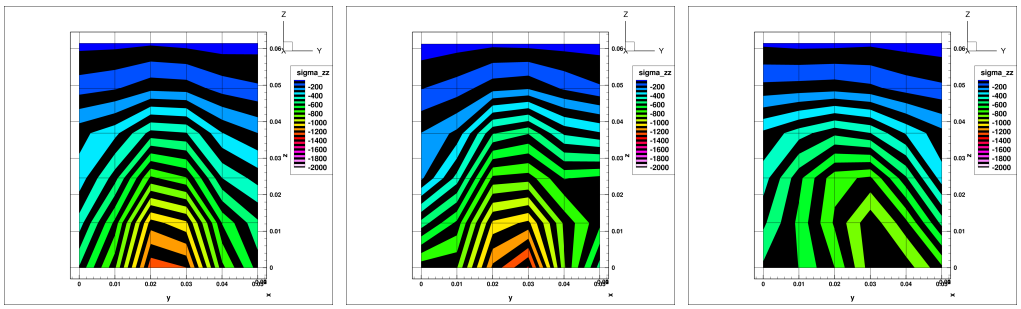

(a) friction. (b) no wall friction. (c) no friction.

Figure 27: Friction effect on σ_{zz} for 7k particle assembly.

The horizontal stress σ_{yy} distribution for the three cases is displayed in Fig.28. Case (b) reveals higher σ_{yy} in the lower-right zone than in case (a), which could be the result of a frictionless wall that allows more re-adjustment between particles in that zone. Case (c) displays even higher concentration

of σ_{yy} in the lower-right corner. The ratio of horizontal to vertical stress σ_{yy}/σ_{zz}, namely, the coefficient of lateral earth pressure at rest K_0, is worthy of more investigation in a separate paper.

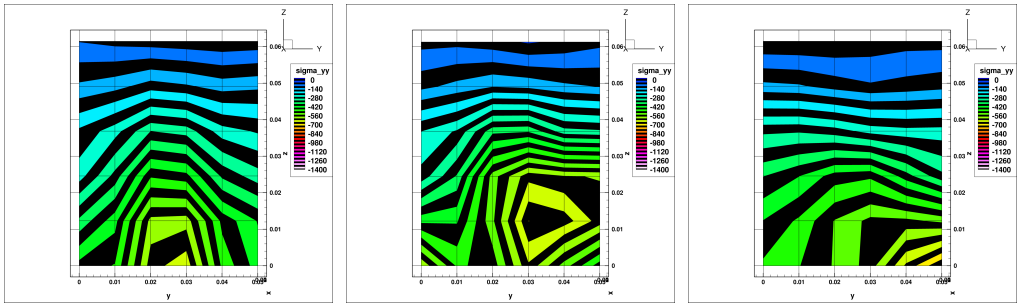

(a) friction. (b) no wall friction. (c) no friction.

Figure 28: Friction effect on σ_{yy} for 7k particle assembly.

The three different friction conditions are also simulated for the 50k particle assembly. The particle assembly motions are displayed at the following YouTube playlist: https://www.youtube.com/playlist?list=PL0Spd0Mtb6vXzsWtvGbiu4w0ukkfL_7J4, where 3 movies play continuously to show the differences. The particle assemblies reveal clear yet distinct dislocations, which can be observed by dot-matrix view shown at the following YouTube playlist: https://www.youtube.com/playlist?list=PL0Spd0Mtb6vUQQjzq7070HokGSkQor8xE. Figure 29 displays the dislocation pattern side view of the 50k particle assembly for the three cases.

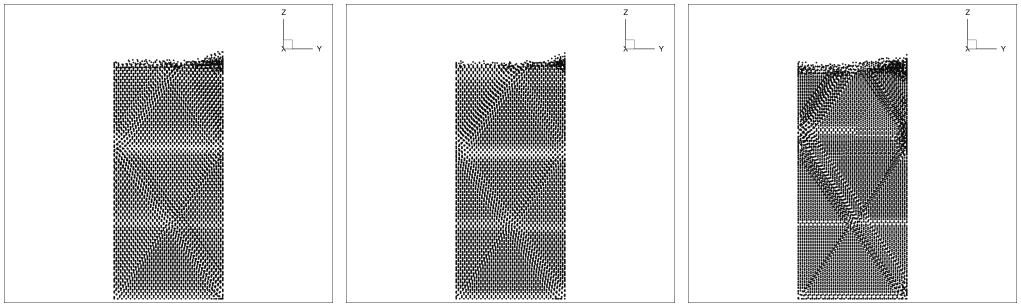

(a) friction. (b) no wall friction. (c) no friction.

Figure 29: Friction effect on dislocations for 50k particle assembly.

Figure 30 displays a slice view of σ_{zz} contour for the 50k particle assem-

bly for the three cases. If comparing (a) friction to (b) no wall friction, the difference may be observed in the lower-right zone, although the overall distributions are similar. Case (c) provides a different stress distribution since it represents a different material with zero friction.

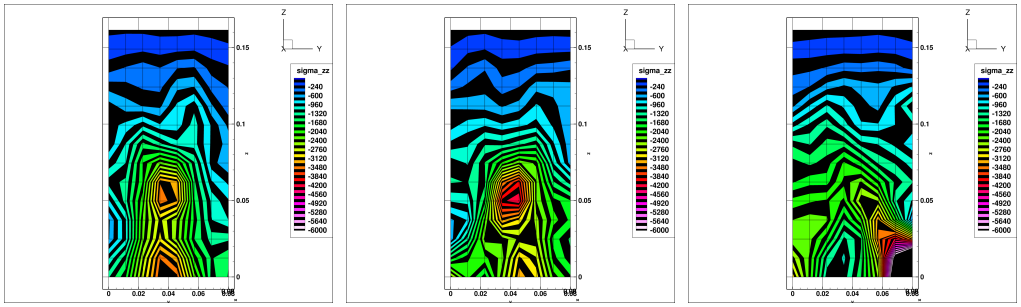

(a) friction. (b) no wall friction. (c) no friction.

Figure 30: Friction effect on σ_{zz} for 50k particle assembly.

From Figs.20, 26 and 29, it is noticed that the monodisperse assemblies tend to "crystallize" by arranging themselves into regular subsets. In our tentative simulations of weak collision using low pluviation/free fall height, the phenomenon is not only observed in monodisperse assemblies of spheres, but also seen in that of ellipsoids; and the flatter the ellipsoids, the weaker the "crystallization." Small-scale polydisperse assemblies have not demonstrated such crystallization, and we do not yet have datasets for large-scale simulations of polydisperse assemblies to analyze. The crystallization phenomenon is worthy of further investigation, which should cover the influence of particle shape, particle size distribution, particle collision strength associated with pluviation height, initial particle spatial distribution, and container side gap space that allows lateral deformation of particle assemblies.

9.3. Influence of particle shape

We hypothesize that particle shape affects the stress distribution resulting from gravitational pluviation. To support this hypothesis, four particle aspect ratios (sphere (1:1:1), ellipsoid-1 (1:0.8:0.6), ellipsoid-2 (1:0.8:0.4), and ellipsoid-3 (1:0.6:0.4)) are used in the pluviation simulations for 250k particles. Each parallel computing grid contains roughly 55 particles. The pluviation processes can be viewed via the following YouTube playlist: https://www.youtube.com/playlist?list=PL0Spd0Mtb6vU_7RwKbiBdpQGS7GGbBvUs. The rested states for the

three aspect ratios of ellipsoidal particles are displayed in Fig.31, in addition to the spherical particles shown in Fig.11(c) (trimmed at the top). Clearly they provide a different structure and packing density due to particle shape difference.

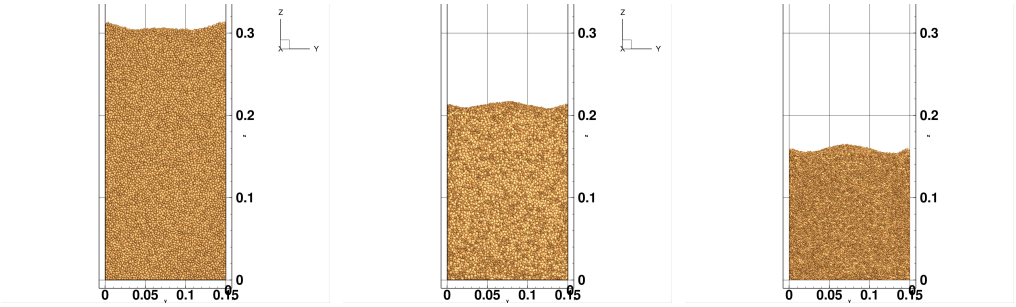

(a) ellipsoid-1. (b) ellipsoid-2. (c) ellipsoid-3.

Figure 31: Particle shape effect on deposited assemblies.

The sphere (Fig.13(c)) and ellipsoid-1 (Fig.32(a)) cases show a dome-shaped σ_{zz} spatial distribution. However, the ellipsoid-2 and ellipsoid-3 cases (Figs.32(b),(c)) exhibit a river plate stress distribution, which shows lower values in the center part of the particle assemblies, contrary to that of dome-shaped distribution. How the distribution is related to particle shapes needs a more comprehensive study involving distributions of localized density or void ratio, principle axis orientations, fabric tensors, spatial topology of particle centroid connectivity and contact point connectivity, etc. But we have recognized that they are related, such that it may be concluded that particle shape affects stress distribution in granular materials.

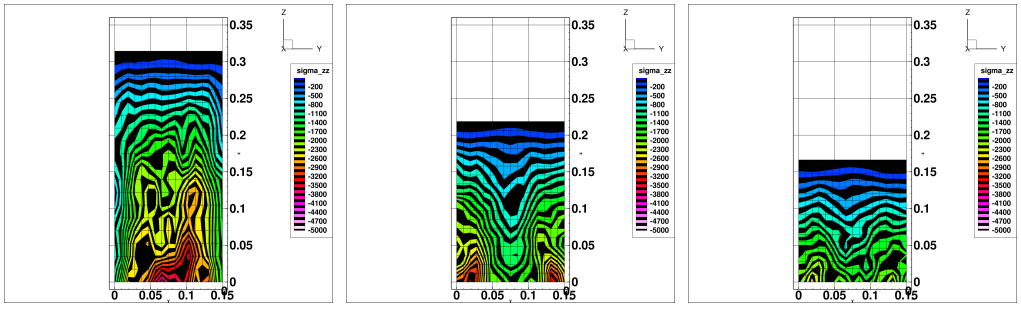

(a) ellipsoid-1. (b) ellipsoid-2. (c) ellipsoid-3.

Figure 32: Particle shape effect on σ_{zz} spatial distribution.

10. CONCLUSION AND OUTLOOK

Bagi's formula is chosen for stress tensor spatial distribution calculation over granular materials under static conditions because (i) it satisfies symmetry, and (ii) a dynamic stress tensor formula, such as *modified Nicot's formula*, converges to it for static equilibrium. Its implementation in MPI parallel computing of 3D DEM is based upon spatial domain decomposition and dynamically-adaptive compute grids, and it requires separate treatment in calculating the internal and external contact forces and corresponding branch vectors. Numerical simulations verify the correctness of implementation in the MPI parallel 3D DEM code *ParaEllip3d* by showing that stress tensors calculated within each grid for parallel computing satisfy symmetry under static conditions.

The combination of stress tensor calculation and large-scale parallel computing provides deeper insight into the micromechanical behavior (stress tensor in the paper) of granular materials under static and dynamic conditions. The normal stress components in gravitationally-deposited particle assemblies exhibit non-uniform spatial distributions under static equilibrium, and the manner by which the maximum stress zone changes during the process of gravitational pluviation and collapse is also captured. 3D DEM simulations illustrate the effect of the following factors on stress distribution: pluviation impact extent, boundary friction, interparticle friction, boundary constraint conditions, and particle shape. Some of the factors, e.g., pluviation height and particle shape, have important engineering implications and are worthy of further study.

It is of great interest and importance to extend the average Cauchy stress tensor calculation in MPI parallel 3D DEM to include finite strain measures, and relevant objective-rate-forms such as Oldroyd and Truesdell stress rates (which involve the velocity gradient) utilizing the compute grids. They will allow a complete mechanical upscaling framework from grain-scale to continuum-scale for the study of stress-strain and stress-strain-rate-form constitutive relations. In future work, a method will be presented to calculate strains, strain-rates, and objective stress-rates for large deformations within granular materials based upon MPI parallel 3D DEM for non-spherical particles.

Acknowledgments

This work was supported by ONR MURI grant N00014-11-1-0691 and ONR

grant N00014-17-1-2704, whose support is gratefully acknowledged. We would like to also acknowledge the DoD High Performance Computing Modernization Program (HPCMP) for granting us the computing resources required to conduct this work. We declare that there is no conflict of interest.

Katalin Bagi. Stress and strain in granular assemblies. *Mechanics of materials*, 22(3):165–177, 1996.

Katalin Bagi. Microstructural stress tensor of granular assemblies with volume forces. *Journal of Applied Mechanics*, 66(4):934–936, 1999.

Katalin Bagi. Discussion on the asymmetry of stress in granular media by jp bardet and i. vardoulakis:[int. j. solids and structures, vol. 38, pp. 353–367 (2001)]. *International Journal of Solids and Structures*, 40(5):1329–1331, 2003.

R Balevičius and D Markauskas. Numerical stress analysis of granular material. *Mechanics*, 66(4):12–17, 2007.

JP Bardet and I Vardoulakis. The asymmetry of stress in granular media. *International Journal of Solids and Structures*, 38(2):353–367, 2001.

John W Baugh Jr and RKS Konduri. Discrete element modelling on a cluster of workstations. *Engineering with Computers*, 17(1):1–15, 2001.

Ching S Chang and Lun Ma. A micromechanical-based micropolar theory for deformation of granular solids. *International Journal of Solids and Structures*, 28(1):67–86, 1991.

J. Christoffersen, M.M. Mehrabadi, and S. Nemat-Nasser. A micromechanical description of granular material behavior. *Trans. ASME, J. App. Mech.*, 48:339–344, 1981.

SC Cowin. Effective stress strain relations for finitely deformed inhomogenous bodies. *Mechanics Research Communications*, 4(3):163–169, 1977.

PA Cundall and ODL Strack. Modeling of microscopic mechanisms in granular material. In *Studies in Applied mechanics*, volume 7, pages 137–149. Elsevier, 1983.

Peter A Cundall and Otto DL Strack. A discrete numerical model for granular assemblies. *Geotechnique*, 29(1):47–65, 1979.

Gery De Saxcé, Jérôme Fortin, and Olivier Millet. About the numerical simulation of the dynamics of granular media and the definition of the mean stress tensor. *Mechanics of Materials*, 36(12):1175–1184, 2004.

Gary W Delaney, Paul W Cleary, Matt D Sinnott, and Rob D Morrison. Novel application of dem to modelling comminution processes. In *IOP Conference Series: Materials Science and Engineering*, volume 10, page 012099. IOP Publishing, 2010.

A Drescher and G De Josselin De Jong. Photoelastic verification of a mechanical model for the flow of a granular material. *Journal of the Mechanics and Physics of Solids*, 20(5):337–340, 1972.

O Durán, NP Kruyt, and S Luding. Micro-mechanical analysis of deformation characteristics of three-dimensional granular materials. *International Journal of Solids and Structures*, 47(17):2234–2245, 2010.

A.C. Eringen. Theory of Micropolar Elasticity. In H. Liebowitz, editor, *Fracture, An Advanced Treatise*, volume 2, pages 622–729. Academic Press, 1968.

Jérôme Fortin, Olivier Millet, and Gery De Saxcé. Construction of an averaged stress tensor for a granular medium. *European Journal of Mechanics-A/Solids*, 22(4):567–582, 2003.

Ian Foster. *Designing and building parallel programs*. Addison Wesley Publishing Company Reading, 1995.

David S Henty. Performance of hybrid message-passing and shared-memory parallelism for discrete element modeling. In *Proceedings of the 2000 ACM/IEEE conference on Supercomputing*, page 10. IEEE Computer Society, 2000.

W Huang, K Nübel, and E Bauer. Polar extension of a hypoplastic model for granular materials with shear localization. *Mechanics of Materials*, 34 (9):563–576, 2002.

Matthew R Kuhn. Discussion of the asymmetry of stress in granular media:[jp bardet and i. vardoulakis, int. j. solids struct. 2001, vol. 38, no. 2, pp. 353–367]. *International journal of solids and structures*, 40(7):1805–1807, 2003.

Keng-Wit Lim and José E Andrade. Granular element method for three-dimensional discrete element calculations. *International Journal for Numerical and Analytical Methods in Geomechanics*, 38(2):167–188, 2014.

Jia Lin and Wei Wu. Asymmetry of the stress tenor in granular materials. *Powder Technology*, 293:113–120, 2016.

Algirdas Maknickas, Arnas Kačeniauskas, Rimantas Kačianauskas, Robertas Balevičius, and Algis Džiugys. Parallel dem software for simulation of granular media. *Informatica*, 17(2):207–224, 2006.

Tang-Tat Ng. Numerical simulations of granular soil using elliptical particles. *Computers and geotechnics*, 16(2):153–169, 1994.

Tang-Tat Ng. Triaxial test simulations with discrete element method and hydrostatic boundaries. *Journal of engineering mechanics*, 130(10):1188–1194, 2004.

François Nicot, Nejib Hadda, Mohamed Guessasma, Jerome Fortin, and Olivier Millet. On the definition of the stress tensor in granular media. *International Journal of Solids and Structures*, 50(14):2508–2517, 2013.

E. Onate and J. Rojek. Combination of discrete element and finite element methods for dynamic analysis of geomechanics problems. *Comp. Meth. App. Mech. Engr.*, 193(27-29):3087 – 3128, 2004. ISSN 0045-7825.

John F. Peters, Mark A. Hopkins, Raju Kala, and Ronald E. Wahl. A polyellipsoid particle for nonspherical discrete element method. *Engineering Computations*, 26(6):645–657, 2009.

L. Rothenburg and A.P.S. Selvadurai. Micromechanical definition of the Cauchy stress tensor for particulate media. In A.P.S. Selvadurai, editor, *Mechanics of Structured Media*, pages 469–486. Elsevier Scientific, 1981.

Lee M. Taylor and Dale S. Preece. Simulation of blasting induced rock motion using spherical element models. *Engineering Computations (Swansea, Wales)*, 9(2):243 – 252, 1992. ISSN 0264-4401.

Vinodh Vedachalam and Davy Virdee. Discrete element modelling of granular snow particles using liggghts. *M. Sc., University of Edinburgh*, 2011.

David W Washington and Jay N Meegoda. Micro-mechanical simulation of geotechnical problems using massively parallel computers. *International journal for numerical and analytical methods in geomechanics*, 27 (14):1227–1234, 2003.

J Weber. Recherches concernant les contraintes intergranulaires dans les milieux pulvérulents. *Bulletin de Liaison des Ponts-et-chaussées*, 20:1–20, 1966.

Christian Wellmann, Claudia Lillie, and Peter Wriggers. A contact detection algorithm for superellipsoids based on the common-normal concept. *Engineering Computations*, 25(5):432–442, 2008.

Beichuan Yan. Three-dimensional discrete element modeling of granular materials and its coupling with finite element method. Technical report, Thesis (Ph.D.)–University of Colorado, 2008.

Beichuan Yan and Richard Regueiro. Comparison between o(n2) and o(n) neighbor search algorithm and its influence on superlinear speedup in parallel discrete element method (dem) for complex-shaped particles. *Engineering Computations*, 35(6):2327–2348, 2018a.

Beichuan Yan and Richard Regueiro. Large-scale dynamic and static simulations of complex-shaped granular materials using parallel three-dimensional discrete element method (dem) on dod supercomputers. *Engineering Computations*, 35(2):1049–1084, 2018b.

Beichuan Yan and Richard A Regueiro. A comprehensive study of mpi parallelism in three-dimensional discrete element method (dem) simulation of complex-shaped granular particles. *Computational Particle Mechanics*, 5 (4):553–577, 2018c.

Beichuan Yan and Richard A. Regueiro. Definition and Symmetry of Averaged Stress Tensor in Granular Media and its 3D DEM Inspection Under Static and Dynamic Conditions. In review, 2018d.

Beichuan Yan and Richard A. Regueiro. Comparison between Pure MPI and Hybrid MPI-OpenMP Parallelism for Three-dimensional Discrete Element

Method (DEM) of Ellipsoid-like Complex-shaped Particles. *Computational Particle Mechanics*, 2018e.

Beichuan Yan and Richard A Regueiro. Superlinear speedup phenomenon in parallel 3d discrete element method (dem) simulations of complex-shaped particles. *Parallel Computing*, 2018f.

Beichuan Yan, Richard A Regueiro, and Stein Sture. Three-dimensional ellipsoidal discrete element modeling of granular materials and its coupling with finite element facets. *Engineering Computations*, 27(4):519–550, 2010.

Boning Zhang and Richard A Regueiro. On large deformation granular strain measures for generating stress–strain relations based upon three-dimensional discrete element simulations. *International Journal of Solids and Structures*, 66:151–170, 2015.

Boning Zhang, Richard Regueiro, Andrew Druckrey, and Khalid Alshibli. Construction of poly-ellipsoidal grain shapes from smt imaging on sand, and the development of a new dem contact detection algorithm. *Engineering Computations*, 35(2):733–771, 2018.